Oxygen and magnesium mass-independent isotopic fractionation induced by chemical reactions in plasma

François Robert, Marc Chaussidon, Adriana Gonzalez-Cano, Smail Mostefaoui

PNAS
www.pnas.org

Main Manuscript for

Oxygen and Magnesium Mass Independent Isotopic Fractionation Induced by Chemical Reactions in Plasma

François Robert [*, 1], Marc Chaussidon[2], Adriana Gonzalez-Cano[2], Smail Mostefaoui[1]

(1) Institut Origine et Evolution (O&E), Muséum national d'Histoire naturelle, Sorbonne Université, IMPMC-UMR 7590 CNRS, 57 rue Cuvier 75005 Paris, France.

(2) Université de Paris, Institut de physique du globe de Paris, CNRS, F-75005 Paris, France.

*Francois ROBERT

Email: (*) : francois.robert@mnhn.fr

ORCID identifier
F. Robert : 0000-0003-2667-9261

Author Contributions:

F.R. designed the project and run the experiments. F.R. and M.C. wrote the paper and interpretation. S.M. and A.G. analyzed the isotopic composition with the NanoSIMS.

Competing Interest Statement: Authors declare no competing interests.

Classification: Earth, Atmospheric, and Planetary Sciences, Chemistry

Keywords: Cosmochemistry, Oxygen, Mass Independent Isotope fractionation

This PDF file includes:

Abstract – Significance Statement - Main Text – Materials and Methods – Acknowledgments – References – Figure 1-3 with captions (embedded in the Text) – Schemes 1-3 (embedded in the Text). Supplementary Informations.

Abstract

Enrichment or depletion ranging from -40 to +100% in the major isotopes ^{16}O and ^{24}Mg were observed experimentally in solids condensed from carbonaceous plasma composed of CO_2/$MgCl_2$/Pentanol or N_2O-Pentanol for O and $MgCl_2$/Pentanol for Mg. In NanoSims imaging, isotope effects appear as micrometer size hotspots embedded in a carbonaceous matrix showing no isotope fractionation. For Mg, these hotspots are localized in carbonaceous grains which show positive and negative isotopic effects so that the whole grain has a standard isotope composition. For O, no specific structure was observed at hotspot locations.

These results suggest that MIF (Mass Independent Fractionation) effects can be induced by chemical reactions taking place in plasma. The close agreement between the slopes of the linear correlations observed between $\delta^{25}Mg$ *vs.* $\delta^{26}Mg$ and between $\delta^{17}O$ *vs.* $\delta^{18}O$ and the slopes calculated using the empirical MIF factor η discovered in ozone[1,2] attests to the ubiquity of this process.

Although the chemical reactants used in the present experiments cannot be directly transposed to the protosolar nebula, a similar MIF mechanism is proposed for oxygen isotopes: at high temperature, at the surface of grains, a mass independent isotope exchange could have taken place between condensing oxides and oxygen atoms originated form the dissociation of CO or H_2O gas.

Significance Statement

Paste your significance statement here. Please note that it should not exceed 120 words, but should be at least 50 words in length. It should not include any references.

Both the physical effect and the chemical conditions at the origin of the oxygen isotope variations in the solar system have been a puzzling question for 50 years. The data reported here with a new experimental protocol bring the MIF effect (Mass Independent Fractionation) originally identified on ozone back to the center of the debate. Similarly to Titanium isotopes, we observe that the MIF effect for O and Mg is triggered by redox reactions in plasma. These observations reinforce the idea of a universal mechanism observable in photochemical reactions when molecular collisions involving indistinguishable isotopes yield a symmetrical complex stabilized as a chemical product.

Main Text

Introduction

Since their discovery in 1973 in the Calcium-Aluminium rich inclusions of the carbonaceous chondrites[3], it has been shown that large enrichments and depletions in ^{16}O were ubiquitous in the solar system, among meteorites, terrestrial planets and the Sun[4-6] and a prominent feature of atmospheric chemistry[7-10]. They were evidenced from the fact that, in a three oxygen isotopes diagram, nearly all solar system samples have isotopic compositions (reported in ‰ variations as $\delta^{17}O$ versus $\delta^{18}O$ values, $\delta^{m}O_{sample} = [(R_{sample}/R_{standard}) - 1) \times 1000$; with $R = {}^{m}O/{}^{16}O$ and m = 17 or 18) defining a linear correlation of slope close to 1 (hereafter referred to as 1:1 CL, the 1 to 1 Correlation Line), instead of a slope 0.52 for the "classical" mass dependent isotopic fractionations (MDF) known to occur during physical and chemical processes[11]. The question of the origin of the 1:1 CL is central to the formation of solids in the early solar system. It has been successively proposed to result from: (i) the injection in the protosolar nebula (PSN) of pure ^{16}O of supernovae origin[3], (ii) a mass independent fractionation (MIF) effect analogous to those observed experimentally during the synthesis of ozone[1,7], and (iii) a self-shielding effect on the solar (or non-solar) UV light by CO[12-14]. While the lack of presolar grains enriched in ^{16}O makes the first proposal unlikely[15], the two other ones have gained some recent theoretical[14,16] or experimental[17,18] support. In the present paper, we address experimentally several issues raised by the ozone experiment to explore whether this 1:1 CL could be due to MIFs reactions having taken place in the PSN.

The formation of ozone results from a three-body reaction. However, at high temperature in a PSN dominated by H_2, the low concentration of elements heavier than H mean that three-body reactions cannot play an important role in the gas phase[16]. In order to overcome this difficulty, the surfaces of growing grains were proposed as possible catalysts for the reactions leading to a MIF effect[16]. Experimental evidence of this effect were reported for $SiO/O_2/H_2$ mixtures[17] but with variations of smaller magnitude than in solar system materials. The present paper is an additional test of this theoretical proposal.

Experimental

Because of the difficulties to carry out controlled condensation experiments in hot plasmas, our approach was not intended to mimic the conditions of the PSN but to answer specific questions having key implications for cosmochemistry. Are oxygen MIFs linked to a precise class of chemical reactions? Are they restricted to gas phase reactions or, as suggested by[18], can they take place during condensation of solids from a gas or be transferred from the gas to condensing solids? Can

the conditions of the appearance of MIFs in the laboratory be reasonably extended to the conditions prevailing in the PSN? To this aim, we investigated reactions involving the isotopes of the two major elements constituting the telluric planets, O and Mg. The comparison between isotopic effects on O and Mg will bring important constraints because, at variance with O, all Mg isotopic fractionations in meteorites are considered to result from MDF processes such as evaporation, condensation and diffusion[19-22].

We have explored different reactions taking place in plasmas between gaseous species leading to the condensation of O and Mg bearing compounds. A summary of these experiments is shown in Table S1. Here we report only the results of experiments that have yielded MIF effects. The experimental protocol is comparable to that previously described for H or Ti[18, 23] and is detailed in Material and Methods.

In microwave plasma, the molecules are dissociated by electron impact producing highly reactive radicals. The high temperature of the gas enhances the rates of chemical or isotopic reactions. In addition, this type of plasma allows the condensation of enough material for isotopic analyses. The aim of these plasma experiments was to produce isotopic exchanges combined with chemical reactions. For oxygen isotopes we studied the reactions between Pentanol and N_2O or between a solution of Pentanol-$MgCl_2$ and CO_2. The radical O atoms, produced by the dissociation of CO_2 or N_2O, react with their parent molecules and an isotopic exchange between O and CO_2 or between O and N_2O can take place. These isotopic exchanges are mediated by the transient formation of the activated complexes $[CO_3]^*$ or $[N_2O_2]^*$. For magnesium isotopes we studied the reaction between Pentanol and $MgCl_2$ for which the isotopic exchange can take place between Mg and $MgCl_2$ through the transient formation of the complex $[Mg_2Cl_2]^*$. The purpose of the introduction of Pentanol along with the O and Mg gaseous carriers, is to produce carbonaceous $C_xH_y^\bullet$ radicals[23,24] (dot designates radicals) that can react with the activated complexes before their dissociation as $O+CO_2$, $O+N_2O$ or $Mg+MgCl_2$. The reaction of the activated complex with a carbonaceous radical should lead to the retrieval of O and Mg from the gas by condensation via the polymerization of organic $C_xH_y^\bullet$-O or $C_xH_y^\bullet$-Mg macromolecules. A MIF effect is predicted in such a case, when an activated complex is involved in two chemical reactions (here dissociation or reaction with $C_xH_y^\bullet$ radicals) at the same time because the rate of a chemical reaction involving a complex formed by identical isotopes is not the same than that of a complex formed by non-identical isotopes[25]. Note that there is no scientific consensus on this interpretation[26].

Results

The Mg and O isotope compositions were measured using NanoSIMS at the Museum National d'Histoire Naturelle in Paris (cf. Table S2 for instrumental setup). A selection of the data is reported

in Table S3 Tables and Figures. NanoSIMS analyses of the majority of the plasma deposited carbonaceous material (PDCM) exhibit small isotopic variability, on the order of 10-30‰, likely due to analytical effects caused by surface sample roughness. In the following, PDCM will refer to this large fraction of condensed organic macromolecules that does not show any significant MIF effect. The measured isotopic variations are thus expressed in δ units using the average isotopic compositions (for O and Mg) of the PDCM as reference values. This procedure allows to minimize analytical matrix effects and to express the isotopic fractionation relative to the non-fractionated compounds produced from the same gas. Analyses of terrestrial samples with no MIF (San Carlos olivine and terrestrial kerogen) and of the PDCM show an external reproducibility (measured in a 10 μm^2 area) of ±≈20‰ (2σ) for δ^{25-26}Mg and ±≈30‰ (2σ) for δ^{17-18}O (cf. Table S3.1, Figure S3.1 and Table S3.3 Figure S3.3).

The Mg and O isotopic results (Figures 1 and 2 constructed from Tables S3.2, S3.4 and S3.5) show four major features. (i) Large MIFs distributing along a line of slope close to 1 are observed both for O and Mg in the experimental condensates. For Mg (Figure 1a) the observed slope (1.127±0.034) is close to the calculated one (0.98 if mass dependent effects are ignored cf. S4) using the model developed for MIF in ozone[18,25]. Similarly, for O, the observed slopes (1.086 ±0.048 for $\delta^{17,18}$O<0‰ and 1.066±0.079 for $\delta^{17,18}$O>0‰, ignoring data with δ^{18}O>250‰) are close to the calculated one (1.00). Note that no free parameter is involved in the calculation of these slopes. (ii) MIFs appear specific to chemical reactions. In Figure 2a, the negative δ^{17}O-δ^{18}O data correspond to the oxidation of Pentanol by N_2O (see also Figure S5), while the positive ones correspond to the oxidation of the Pentanol/$MgCl_2$ solution by CO_2. In the Pentanol/$MgCl_2$/CO_2 experiment, one area on the Si wafer shows variations distributed along a slope ≈0.5 but with an enormous range of variations in δ^{18}O (from ≈+700 to ≈ +1500‰; Figure 2a) impossible to explain by a "classical MDF" (iii) Oxygen isotopic variations along the 1:1 CL are not correlated to the ^{16}O concentration (i.e. to the ion count rate; cf. Table S3.5), so that they cannot be explained by mixing between 2 components but requires instead variations in the magnitude of the MIF factor producing multiple end-members. (iv) At the scale of 200-500 nm, MIFs are not systematically associated with elemental O hotspots, i.e. with an increase in the ionic emissivity of O compared to that from the amorphous PDCM where no MIF effect is observed. Note that, in the case of the Pentanol/N_2O experiment, no hotspot in emissivity was observed at the location of negative MIF effects.

As reported in Figure 1 in the case of the Pentanol/$MgCl_2$ experiments, isotopic Mg hotspots were clearly associated with the rim of carbonaceous grains (cf.[27] for the formation of nanoparticles from plasma). As observed for Ti isotopes[18], the Mg MIF effect varies within the grains in such a way that the isotopic mass balance is achieved at the scale of the bulk grain. For experiments involving oxygen isotopes, the morphology of the grains carrying the MIF effect could not be

168 determined and it cannot be excluded that the MIF carriers are part of the molecular structure of
169 the PDCM.
170
171
172 **Discussion**
173
174 Several theoretical origins of the MIF effect (i.e. the origin of the MIF factor noted η) have been
175 proposed[26, 28-30]. Here we take for granted that the MIF effect appears when the activated complex
176 responsible for the isotopic exchange is involved in a chemical reaction[6,16,25].
177 For the CO_2/$MgCl_2$/Pentanol experiment, the complex is likely $[CO_3]^*$[31]. Because (i) no oxygen
178 MIF effect is observed in the Penthanol/CO_2 experiment (cf. Table S1) and because (ii) at the
179 location of oxygen MIF, chlorine is observed by SEM as ≈200 nm spots while Mg is absent, the MIF
180 effect is attributed to the reaction of $[CO_3]^*$ with an organochlorine radical (C_xH_y-Cl)$^\bullet$. The complex
181 $[CO_3]^*$ can either decompose and return to the gas (Channel 1 of the following reaction 1) or be
182 stabilized (Channel 2) as (C_xH_y-ClO). In this model both Channels lead to a MIF effect with
183 fractionation opposite in sign, but only the isotopic effect in the condensed phase can be preserved
184 in the reaction products since isotopic re-equilibration will take place in the gas.
185 *Reaction 1.*

186 The lack of measurable MIF effects in the PDCM indicates that C_xH_y-O can also directly
187 condense without reacting with the complex $[CO_3]^*$. We thus now distinguish between two types of
188 condensation: a complex-mediated condensation and a direct condensation (i.e. a two-body
189 reaction). A similar scheme can be proposed to explain the Penthanol/N_2O experiment where the
190 complex would be $[N_2O_2]^*$.

191 The present experimental observations can be tentatively extended to the origin of oxygen
192 isotopic variations in the PSN. A possible scenario - alternative to the self-shielding ones[12-14] - can
193 be proposed (Reaction 2; Figures. 3a, b):

194 *Reaction 2*

195 In this scenario, E is a chemical element (E ≡ Si, Al, Mg, Ca etc..) forming an oxide EO that
196 condenses from the gas phase. O_{Ads} and EO_{Ads} correspond to species adsorbed at the surface of
197 a solid (subscript Ads in Reaction 2) during its condensation, so that the formation rate of $[EO\text{-}O]_{Ads}^*$ is enhanced by many orders of magnitude relative to the rate in gas phase reaction. Note
199 that, contrary to the self-shielding model, the dissociation of H_2O_{Gas} or CO_{Gas} does not produce MIF
200 fractionationed oxygen atoms (O_{Gas}). The oxygen isotope exchange takes place in $[EO\text{-}O]_{Ads}^*$ and
201 produce the MIF effect during its decomposition. The Channel 1 corresponds to the stabilization of
202 a fraction of the complex $[EO\text{-}O]_{Ads}^*$ in the solid (subscript Sol) by unknown reactions. The dashed

arrows for the Channel 2 indicate that the other fraction of the complex $[EO\text{-}O]_{Ads}^{*}$ can be either incorporated in the solid (Channel 2a) as observed here for Mg and for Ti[32] isotopes or can spontaneously dissociate to the gas phase. (Channel 2b). The O returned to the gas by this destabilization of a fraction of the complex, re-equilibrates isotopically with the major oxygen bearing molecules of the PSN (H_2O and CO). The magnitude and the sign of MIF in the two fractions of the complex stabilized in the solid are expected to depend on the type of chemical reaction taking place, as observed in the present experiments with oxidation of pentanol by either N_2O or CO_2 producing either ^{16}O excess or ^{16}O depletion, respectively (Figure 2). In other words, in the PSN, if this process occurs, then different oxides should fractionate differently oxygen isotopes but, possibly in a mass independent manner.

This catalytic property of grain surfaces for enhancing the rate of reaction between adsorbed species, overcomes one of the major difficulties for having MIF effects in the PSN. Indeed, in the PSN, in a large excess of H_2, the O atoms produced by the photodissociation of H_2O or CO[33] are likely to react with H_2 to form OH + H much faster than being involved in a gaseous three body reaction similar to that which leads to ozone[16]. However, the chemical nature of the adsorbed activated complex taking part to condensation reactions in the PSN is, at this stage, impossible to predict. This is exemplified by the fact that no MIF is observed in meteorites for Mg, while large MIFs are produced in our experiments. This may indicate that the possible activated complexes involving two Mg atoms are unstable (such as $[Mg_2O]^*$) in the chemical conditions that prevailed during the condensation of Mg-rich silicates (forsterite could for instance form by direct condensation and not by a complex-mediated condensation).

Thus, assuming that the gas from which the first oxides and silicates condense in the PSN has the isotopic composition measured for the Solar wind ($\delta^{17}O \approx \delta^{18}O \approx$ -60‰)[4,5], only the grains condensed by a complex-mediated condensation would develop MIF effects with $\delta^{17}O \approx \delta^{18}O$ either > -60‰[34] or <-60‰[35,36]. All the other condensates, formed by direct condensation, would have the oxygen isotopic composition of the PSN (Figure 3b). Note however that, due to mass balance effects, a gaseous reservoir previously fractionated by complex-mediated condensation could produce, by direct condensation, solids with MIF effects.

The simultaneous occurrence of these two types of condensation reactions, having different consequences as far as oxygen isotopes are concerned, may account for part of the large diversity of isotopic compositions observed in CAIs and chondrules from primitive meteorites[34]. Note however that the large $\delta^{17}O \approx \delta^{18}O$ variations observed in the present experiments (several hundreds of ‰) compared with the much smaller enrichments in $^{17,18}O$ relative to the Sun observed in most solar system solids (50-70‰) implies that their oxygen isotopic composition contains only a small MIF contribution.

As postulated in the Reaction 2 and observed during the formation of SiO_2[17], complexes[37] resulting from the dissociation of H_2O could be responsible for the extreme ^{16}O depletion ($\delta^{17,18}O$ (‰) up to +180‰) observed[38] in some rare minerals whose synthesis involves the reaction between Fe (or FeS) and H_2O[38] (cf. Figure3b).

Although the self-shielding model remains a viable possibility in the PSN to produce reservoirs variously depleted or enriched in ^{16}O[12, 13], the presently proposed MIF constitutes an additional potential source of ^{16}O enrichments and depletion. This scenario is testable in laboratory through dedicated experiments of high temperature oxide condensation.

Materials and Methods

1- Experimental protocol.

All experiments (cf. the schematic drawing in Figure 4) were performed in a glass line where the pressure reaches 10^{-4} Torr. A gas vector (N_2 for the Mg experiment and N_2O or CO_2 for the oxygen experiments) is injected into the line and passes through a cylinder glass tube (Ø = 1 cm, *l* = 10 cm) where the pressure is maintained at ≈1 Torr by dynamical pumping. Glass reservoirs containing organic liquids (Pentanol or $MgCl_2$ dissolved in Pentanol) were connected to the line by stopcocks. The vapor pressure of the liquids was injected in the gas vector by adjusting the leak of these stopcocks. The gas to organic pressure ratio was of the order of 1:1. The characteristic lifetime of the gas in the tube was 1/10 sec. The plasma was produced in the center of the glass tube by an HF discharge at 2450 MHz. In such conditions, the molecular temperature is estimated to be around 1000K. The plasma is not thermal i.e. the temperature of the electrons is higher than that of the molecules.

Silicon wafers were deposited 5 cm downhill from the discharge. Carbonaceous matter was deposited on the glass walls around the discharge and on the silicon wafers. It was mechanically collected as a powder for isotopic analyses. The molecular organic structure of this carbonaceous matter is described elsewhere[39]. Except for experiments involving N_2O, MIF effects were found on the wafers. Except for Mg, no structural grain corresponding to the size and distribution of isotopic hotspots was identified by SEM.

We report in this paper only experiments where MIF effects were identified (other experiments are listed in Table S1). It should be kept in mind that MIF-bearing grains are rare in the organic matter (named PDCM for Plasma Deposited Carbonaceous Matter for the organic matter with no significant MIF). So, the fact that no MIF region was observed in these samples is not definitive proof that they are absent.

2. Analytical protocol.

The Mg and O isotope compositions were measured using NanoSIMS at the Museum National d'Histoire Naturelle in Paris. The isotopic compositions of individual grains (∅ 0.5 to 2 μm) were analyzed by image analysis using the *l'Image* software package (L. Nittler, Carnegie Institution of Washington, Washington, DC). For NanoSIMS analyses, carbonaceous powder collected on the glass walls (region 4 in Figure 4) were pressed on gold, gold coated and mounted on 1 inch holders. Silicon wafers are gold coated without any further preparation. The instrumental parameters of the NanoSims are reported in Table S2.

In order to have comparable topographic and matrix effects for the isotopic reference and for the samples, all data are reported using the PDCM as the reference value. In others terms, the isotopic fractionation is expressed relative to the carbonaceous deposits that do not show MIF effects in excess of $\approx \pm 2\sigma$ relative to their average value. When analyses were performed randomly, each area ($\approx$ 20×20 μm) was divided in 9 regions (i.e. ROI $\approx$ 6×6 μm; noted "*Random Area"* in Tables S3.3 and S3.5). Data reported in Tables S3.2, 3.4, and 3.5 are used to construct the Figures in the text. Two examples of the distribution of the Mg and O data recorded on the PDCM are shown in Figures S3.1 and S3.3.

Analyses on terrestrial kerogen powders give reproducibility of ±37 and ±23 on $\delta^{17}O$ (‰) and $\delta^{18}O$ (‰), respectively (2σ), similar to those measured for the PDCM. Under the same conditions, the reproducibility on the polished San Carlos olivine standard is $\approx$ ±5 and $\approx$ ±8 on $\delta^{17}O$ (‰) and $\delta^{18}O$ (‰), respectively. The poor reproducibility on the PDCM is caused by the topography of the organic powder pressed in gold, bearing in mind that the presence of non-detected MIF bearing grains cannot be totally excluded.

For magnesium, a synthetic sample (Methylmagnesium chloride evaporated in the air) was used to verify the MDF relations between the electron multipliers. For oxygen, these relations are checked routinely for rock sample analyses.

Acknowledgments

This work was supported by grants from CNRS MITI (ISOTOP 2020, COSMIFs), from ANR (ANR-20-CE49-0011-01). F.R. acknowledges support (Overheads) of ERC Advanced Grant *PaleoNanoLife* (PI: F. Robert; 161764). F.R. designed the project and run the experiments. F.R. and M.C. write the paper and interpretation. S.M. and A.G. analyzed the isotopic composition with the NanoSIMS. We would like to thank Florie Lopis for her availability and efficiency without which the realization of these experiments would not have been possible. Sylvain Pont's contribution was appreciated for SEM analyses.

References

1- M.H. Thiemens, J.E. Heidenreich, The mass-independent fractionation of oxygen - a novel isotope effect and its possible cosmochemical implications. *Science*, 219, 1073-1075 (1983).

2- C. Janssen, J. Guenther, K. Mauersberger, D. Krankowsky, Kinetic origin of the ozone isotope effect: a critical analysis of enrichments and rate coefficients. *Phys. Chem. Chem. Phys.,* **3**, 4718-4721 (2001).

3- R.N. Clayton, L. Grossman, T. K. Mayeda, A component of primitive nuclear composition in carbonaceous meteorites, *Science*, 182, 485–488 (1973).

4- K. Hashizume, M. Chaussidon, A non-terrestrial ^{16}O-rich isotopic composition for the protosolar nebula. Nature 434, 619-621.4, (2005).

5- K. McKeegan, A. P. A. Kallio, V. S. Heber, G. Jarzebinski, P. H. Mao, C. D. Coath, T. Kunihiro, R. C. Wiens, J. E. Nordholt, R. W. Moses Jr., D. B. Reisenfeld, A. J. G. Jurewicz, D. S. Burnett, The Oxygen Isotopic Composition of the Sun Inferred from Captured Solar Wind. *Science*, 332, 1528 (2011).

6- E.D. Young, K. Kuramoto, R.A. Marcus, H. Yurimoto, S.B. Jacobsen, Mass-independent Oxygen Isotope Variation in the Solar Nebula. *Reviews in Mineralogy & Geochemistry*. 68, 187-218 (2008).

7- M.H. Thiemens, Introduction to Chemistry and Applications in Nature of Mass Indepedendent Isotope Effects Special Feature. *PNAS* **110**, 44, 17631-17637 (2013).

8- M.H. Thiemens, M. Lin. Use of Isotope Effects To Understand the Present and Past of the Atmosphere and Climate and Track the Origin of Life. *Angew. Chem. Int.* 58, 6826 –6844 (2019).

9- M. C. Liang, F. W. Irion, J. D. Weibel, G. A. Blake, C. E. Miller, Y. L. Yung, Isotopic composition of stratospheric ozone, *J. Geophys. Res.*,111, D 02302 (2006).

10- A. H. Laskar, S. Mahata, S. K. Bhattacharya, M.-C. Liang, Triple oxygen and clumped isotope compositions of CO_2 in the middle troposphere. *Earth and Space Science*, 6, 1205–1219, (2019).

11- E.D. Young, A. Galy, H. Nagahara, Kinetic and equilibrium mass-dependent isotope fractionation laws in nature and their geochemical and cosmochemical significance. *Geochim. Cosmochimi. Acta*, 66, 1095-1104 (2002).

12- H. Yurimoto, K. Kuramoto, Molecular Cloud Origin for the Oxygen Isotope Heterogeneity in the Solar System. *Science*, 305, 5691, 1763- 1766 (2004).

13- J.R. Lyons, E Young, CO self-shielding as the origin of oxygen isotope anomalies in the early solar nebula. *Nature*, 435, 317- 320 (2005).

14- J.R. Lyons, *Geochim. Cosmochim. Acta*, An analytical formulation of isotope fractionation due to self-shielding. *Science,* **282**, 177-200 (2020).

15- L.R. Nittler, Presolar stardust in meteorites: recent advances and scientific frontiers *Earth. Planet. Sci. Lett.,* 209, 259-273 (2003).

16- R.A. Marcus, Mass-independent isotope effect in the earliest processed solids in the solar system: A possible chemical mechanism. *J. Chem. Phys.* 121, 8201-8211 (2004).

17- S. Chakraborty, P. Yanchulova, M. H. Thiemens, Mass-Independent Oxygen Isotopic Partitioning During Gas-Phase SiO_2 Formation. *Science* 342, 6157, 463-466 (2013).

18- F. Robert, R. Tartese, G. Lombardi, P. Reinhardt, M. Roskosz, B. Doisneau, Z. Deng, M. Chaussidon, Mass-independent fractionation of titanium isotopes and its cosmochemical implications. *Nat. Astron.* 4, 1–7, https://doi.org/10.1038/s41550-020-1043-1 (2020).

19- R. N. Clayton, R. W. Hinton and A. M. Davis, Isotopic Variations in the Rock-Forming Elements in Meteorites. *Phil. Trans. R. Soc. Lond. A*. 325, 483-501 (1988).

20- G.J. MacPherson, A.M. Davis, E. Zinner, The distribution of aluminum-26 in the early Solar System - A reappraisal. *Meteoritics* 30, 365-389 (1995).

21- A. M. Davis, A. Hashimoto, R. N. Clayton, T. K. Mayeda, Isotope mass fractionation during evaporation of Mg_2SiO_4. *Nature* 347, 655-658 (1990).

22. E. D. Young, A. Galy, The Isotope Geochemistry and Cosmochemistry of Magnesium. *Rev. Mineral. Geochem.* **55**, 197–230 (2004).

23- F. Robert, S. Derenne, G. Lombardi, K. Hassouni, A. Michau, P. Reinhardt, R. Duhamel, A. Gonzalez, K. Biron, Hydrogen isotope fractionation in methane plasma. *PNAS* **114** (5), 870-874 (2017).

24- M. Scapinello, E. Delikonstantis, G.D. Stefanidis, The panorama of plasma-assisted non-oxidative methane reforming. *Chemical Engineering - Processing: Process Intensification* 117, 120–140 (2017).

25 - P. Reinhardt, F. Robert, On the mass independent isotopic fractionation in ozone. *J. Chem. Phys.* 513, 287–294 (2018).

26- A. Teplukhin, D. Babikov, Properties of Feshbach and “shape”- resonances in ozone and their role in recombination reactions and anomalous isotope effects. *Faraday Discuss*., **212**, 259 (2018). DOI: 10.1039/c8fd00089a.

27- A. B. Murphy, Formation of titanium nanoparticles from a titanium tetrachloride plasma. J. *Phys.Appl. Phys* . 37 2841–2847 (2004).

28- Y.Q. Gao, R.A. Marcus, On the theory of the strange and unconventional isotopic effects in ozone formation. *J. Chem. Phys.* **116**, 137 (2002).

29- R. Schinke, P. Fleurat-Lessard, The effect of zero-point energy differences on the isotope dependence of the formation of ozone : a classical trajectory study. *J. Chem. Phys*., **122**, 094317 (2005).

30- M.V. Ivanov, D. Babikov, On molecular origin of mass-independent fractionation of oxygen isotopes in the ozone forming recombination reaction. *PNAS* 110 (44) 17708-17713 (2013).

31- B. L. Grigorenko, L. Duarte, I.V. Polyakov, A.V. Nemukhin, Theoretical characterization of the photochemical reaction $CO_2 + O(3P) \rightarrow CO + O_2$ related to experiments in solid krypton *Chem. Phys. Lett*, 746, 137303 (2020).

32- F. Robert, P. Reinhardt, R. Tartese, Mass-independent fractionation of titanium isotopes. *Chem. Phys*. 540, 110970 (2021).

33- M. L. Ovcharov, V. M. Granchak, Photocatalytic activation of carbon monoxide on semiconductors and derived nanocomposites: basic principles and mechanisms: a review *Theoretical and Experimental Chemistry*, 55, 3, DOI 10.1007/s11237-019-09608-3 (2019).

34- A. N. Krot, K. Nagashima, J. R. Lyons, J-E Lee, M. Bizzarro, Oxygen isotopic heterogeneity in the early Solar System inherited from the protosolar molecular cloud *Science Advances*, 6, 42, DOI: 10.1126/sciadv.aay2724 (2020).

35- S. Kobayashi, H. Imai, H. Yurimoto, *Geochem. J.* New extreme ^{16}O-rich reservoir in the early solar system. 37, 663-669 (2003).

36- M. Gounelle, A. N. Krot, K. Nagashima, A. Kearsley, Extreme ^{16}O enrichment in calcium–aluminum-rich inclusions from the Isheyevo(ch/cb) chondrite. *Ap. J.* 698, L12–L22 (2009).

37- S. Pehkonen, K. Marushkevich, L. Khriachtchev, M. Räsänen, B.L. Grigorenko, A.V. Nemukhin, Photochemical Synthesis of H_2O_2 from the $H_2O{\cdot}O(^3P)$ van der Waals Complex: Experimental Observations in Solid Krypton and Theoretical Modeling. *J. Phys. Chem. A* 111 11444–11449 (2007).

38- N. Sakamoto, Y. Seto, S. Itoh, K. Kuramoto, K. Fujino, K. Nagashima, A.N. Krot, H. Yurimoto, Remnants of the Early Solar System Water Enriched in Heavy Oxygen Isotopes. *Science*, 317, 231-233 (2007).

39 - K. Biron, S. Derenne, F. Robert, J.N. Rouzaud, Toward bab experimental synthesis of the chondritic insoluble organic matter. *MAPS,* **50**, Nr 8, 1408-1422 (2015).

411

412 **Figure Legends**

413 **Figure 1**: (a) Magnesium isotopic compositions of Mg-bearing carbonaceous grains reported as
414 δ^{25}Mg *vs.* δ^{26}Mg variations relative to the PDCM (0:0 ±≈20‰). Data were collected in 4 grains either
415 as surface or volume variations (cf. Table S3.2). Error bars include statistical errors (ion counting
416 statistic) and the reproducibility on the standard (±2σ). The 1:1 dashed line is drawn for reference
417 but does not stand for the best fit line to the data.
418 (b) δ^{26}Mg and δ^{25}Mg variations of the rim of the 5 μm size grain shown in Figure1c are reported
419 as a function of the analytical sputtering time expressed in sec (data also reported in Figure 1a).
420 The total sputtering duration (6600 sec) indicates that the rim of the grain is ≈200 nm thick. The
421 PDCM (δ^{26}Mg ≈ δ^{25}Mg ≈0‰) embedding the grain reappears after complete sputtering. Note the
422 two-outlier data (which are not analytical errors) observed during the flipping from negative to
423 positive δ values (also obvious in Figure 1a). Cf. sample *Robert-Juillet-2019_23.im* in Table S3.2.
424 (c) Ionic image of the distribution of δ^{26}Mg shown in Figure 1b. This image is made by the
425 summation of the 3 scans collected between 3600 and 4800 sec (cf. Figure 1b). The core of the
426 grain (in blue) has a homogeneous isotopic composition (δ^{26}Mg≈δ^{25}Mg≈0‰) while the rim exhibits
427 marked enrichments in ^{26}Mg (^{25}Mg not reported here) localized in spots that do not exceed 200 nm
428 in size. The PDCM where the δ^{25}Mg and δ^{26}Mg cannot be defined because of the too low counting
429 rates on ^{25}Mg and ^{26}Mg appears in black.
430 (d) SEM image of another Mg-bearing carbonaceous grains (not analyzed for isotopic analyses)
431 deposited on the silicon wafers. The structure suggests that the extreme isotopic variations
432 observed in the grain shown in (c) are concentrated in the fine-grained rim.
433
434
435 **Figure 2**: Figure 2a: Oxygen isotopic compositions of grains embedded in the PDCM are
436 reported as δ^{17}O *vs.* δ^{18}O. The δ variations are expressed relative to PDCM (0-0‰ ± ≈30‰; 2σ).
437 Error bars include statistical errors (ion counting statistic) and the reproducibility on the standard
438 (±2σ). Open diamonds stand for the oxidation of Pentanol by N_2O. Open and black dots stand for
439 the oxidation of the $MgCl_2$/Pentanol solution by CO_2 (open dots for grains concentrated in the same
440 100×100 μm area and defining a slope≈0.5). The 1:1 dashed line is drawn for reference, not for
441 the best fit line. The correlation defined by the black dots does not intercept at 0-0‰; this can be
442 an analytical matrix effect or a MDF contribution to the MIF effect.
443 Figure 2b: NanoSims ion image (20×20 μm; sample *Robert-Juillet-2020_9* in Table S3.5)
444 showing four hotspots in oxygen intensities where MIF compositions were measured and reported
445 in Figure S6 (PDCM in black). The measured δ^{17}O are reported on the figure for 3 of the 4 hotspots.
446 In order to increase the contrast of the image the colors vary according to the logarithmic intensity
447 of the count rate (Cps for counts/sec).
448 Figure 2c. NanoSims ion image (20×20 μm; sample *Robert-Juillet-2020_18* in Table S3.5)
449 showing isotopic hotspots on Si wafer (in δ^{18}O(‰) units).
450

451 **Figure 3:** (a) δ^{17}O *vs.* δ^{18}O diagram for the solar system. Selection of observational constraints.
452 The MDF line (slope 0.52) is shown for the Earth-Moon system (dashed line). Minerals from
453 refractory inclusions (CAIs), ameboid olivine aggregates (AOAs) and chondrules in carbonaceous
454 chondrites define the 1:1 CL. Sun: $\delta^{17,18}$O ≈ -60‰[(5)]. Some rare CAIs, relict CAIs in chondrules and

chondrule from CH-CB chondrites are enriched in ^{16}O relative to the Sun[35,36]. Extreme ^{16}O depletion was observed in the C3-Acfer 094 meteorite[38]. Most meteorites (Chondrites H, L and LL), the Earth, Moon and Mars have bulk $\delta^{17,18}O$ values around 0±10‰.

(b) Qualitative interpretation of (a). The PSN gas has the oxygen isotopic composition of the Sun: $\delta^{17,18}O \approx$ -60‰. The position of the grains on the 1:1 line is, at first order, dictated by the chemical reaction responsible for the complex-mediated condensation of oxides and silicates (noted $[EO_2]^*$ with E designating Si, Mg, Al etc.). Oxides would exhibit either ^{16}O depletion or enrichment relative to the Sun. The extreme ^{16}O depletion observed in the C3-Acfer 094 meteorite could result from a reaction involving one of the $[O\text{-}H_xO]^*$ complexes resulting from the dissociation of H_2O[37]. Condensation taking place without going through an activated complex (noted direct condensation) should yield grains having the oxygen isotopic composition of the ambient gas, which can be different from the Sun if this gas was previously fractionated by complex-mediated condensation.

Figure 4: (1) gas vector (N_2 or N_2O or CO_2) (2) reservoir of organic liquids (Pentanol or Pentanol-$MgCl_2$) (3) leak of (2) in (1) (4) Microwave cavity (5) Silicon Wafer. Organic deposits are present on the glass walls of region 4 and on the Wafer.

Reaction Legends

Reaction 1: Possible reaction at the origin of the oxygen MIF effect observed in the CO_2/$MgCl_2$/Pentanol plasma experiment.

Reaction 2: Proposed chemical scheme at the origin of the mass independent oxygen isotopic reaction observed in solar system materials.

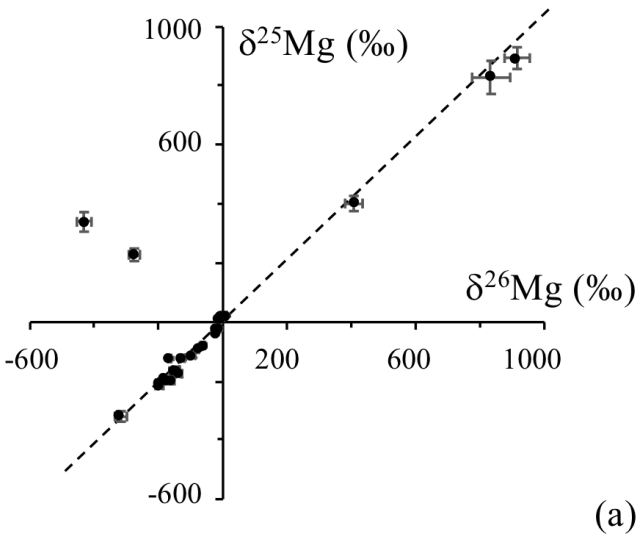
1000
600
δ25Mg (‰)
δ26Mg (‰)
-600
200
600
1000
-600
(a)

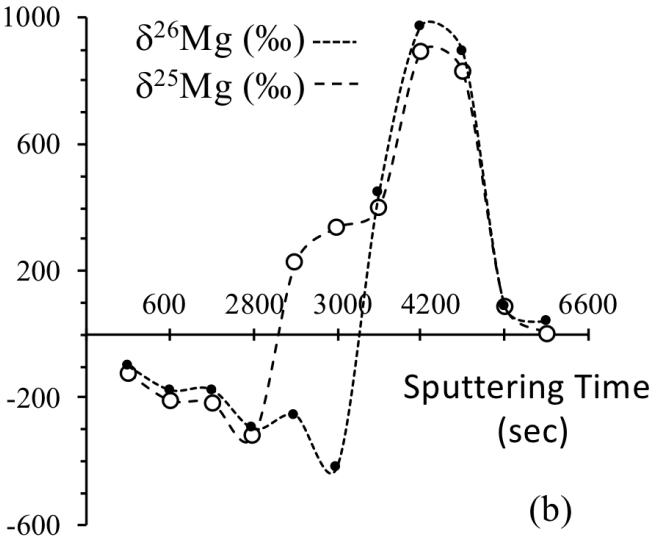
1000
600
200
-200
-600
δ26Mg (‰)
δ25Mg (‰)
600
2800
3000
4200
6600
Sputtering Time
(sec)
(b)

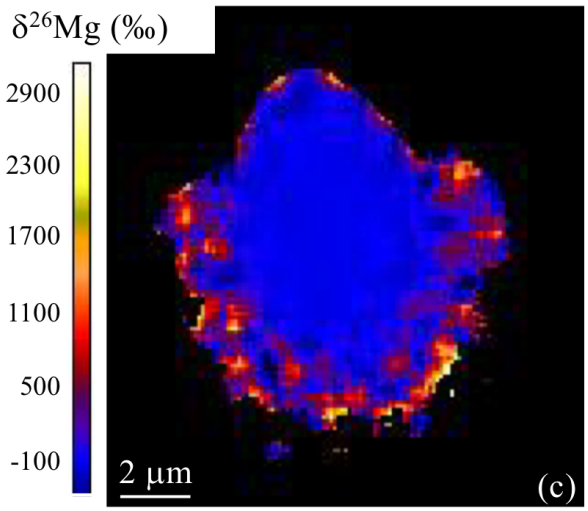
δ26Mg (‰)
2900
2300
1700
1100
500
-100
2 μm
(c)

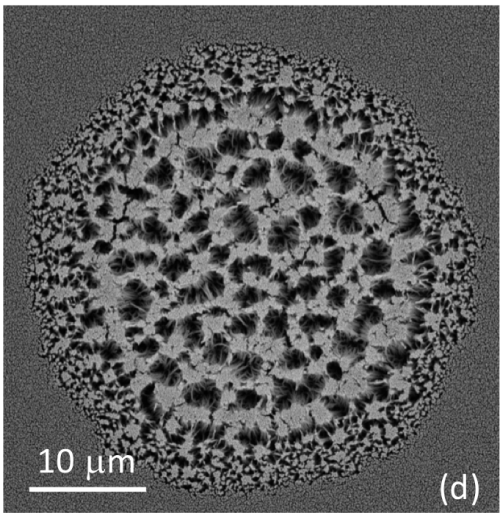
10 μm
(d)

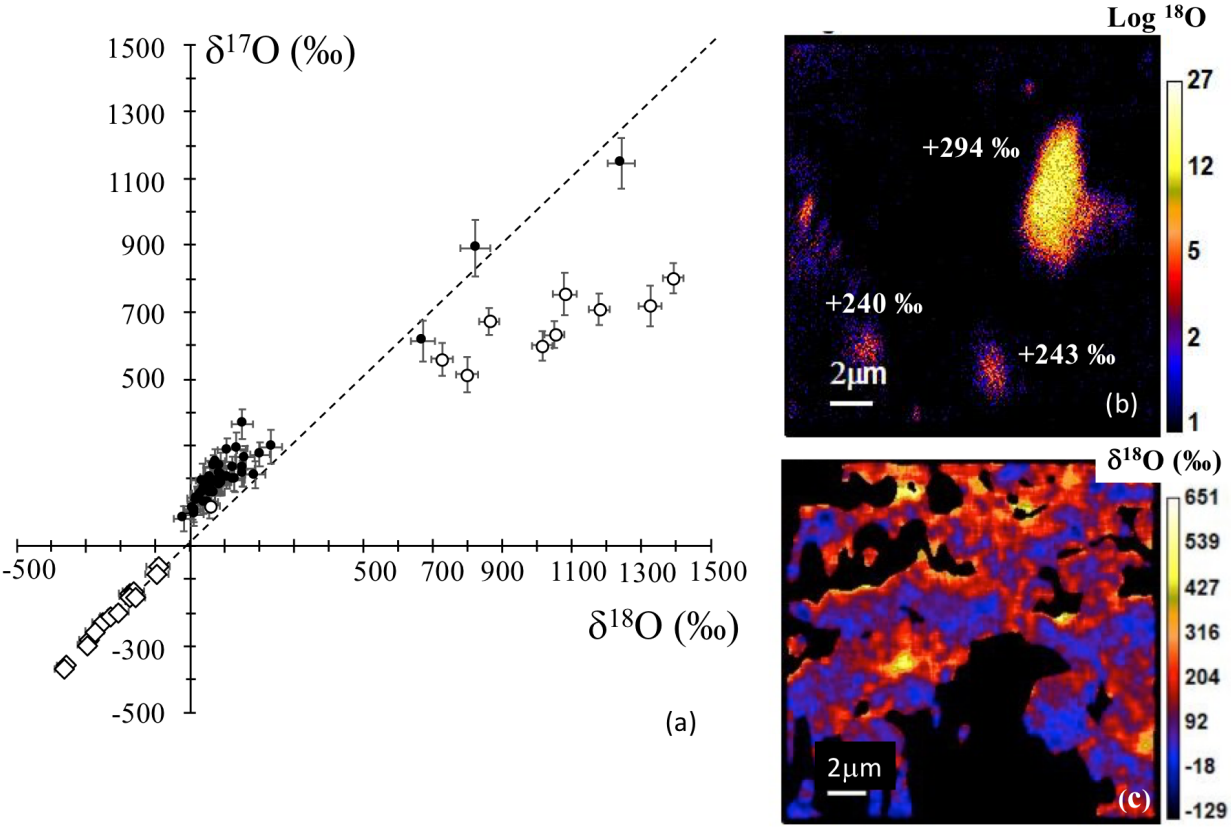
1500
1300
1100
900
700
500
-500
-300
-500
500 700 900 1100 1300 1500
δ17O (‰)
δ18O (‰)
(a)
Log 18O
27
12
5
2
1
+294 ‰
+240 ‰
+243 ‰
2µm
(b)
δ18O (‰)
651
539
427
316
204
92
-18
-129
2µm
(c)

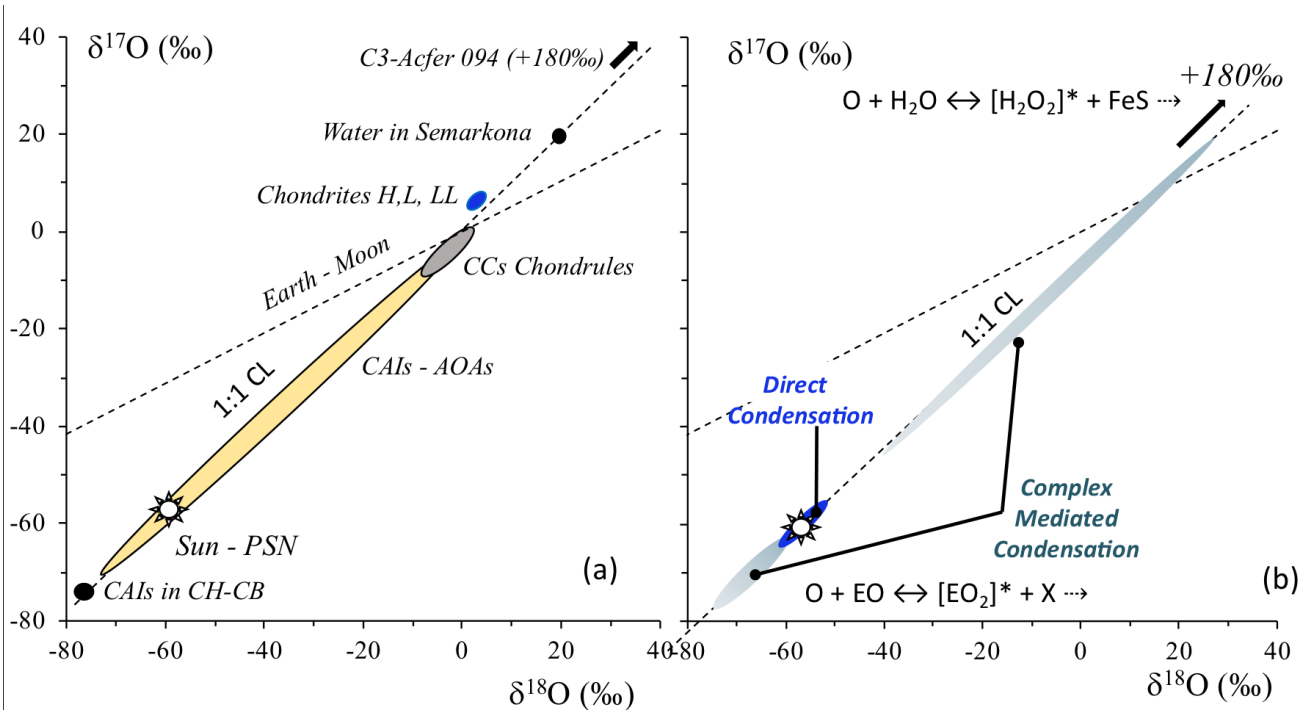
δ17O (‰)
C3-Acfer 094 (+180‰)
Water in Semarkona
Chondrites H,L, LL
Earth - Moon
CCs Chondrules
1:1 CL
CAIs - AOAs
Sun - PSN
CAIs in CH-CB
(a)
δ18O (‰)
δ17O (‰)
+180‰
O + H2O ↔ [H2O2]* + FeS ⇢
1:1 CL
Direct Condensation
Complex Mediated Condensation
O + EO ↔ [EO2]* + X ⇢
(b)
δ18O (‰)

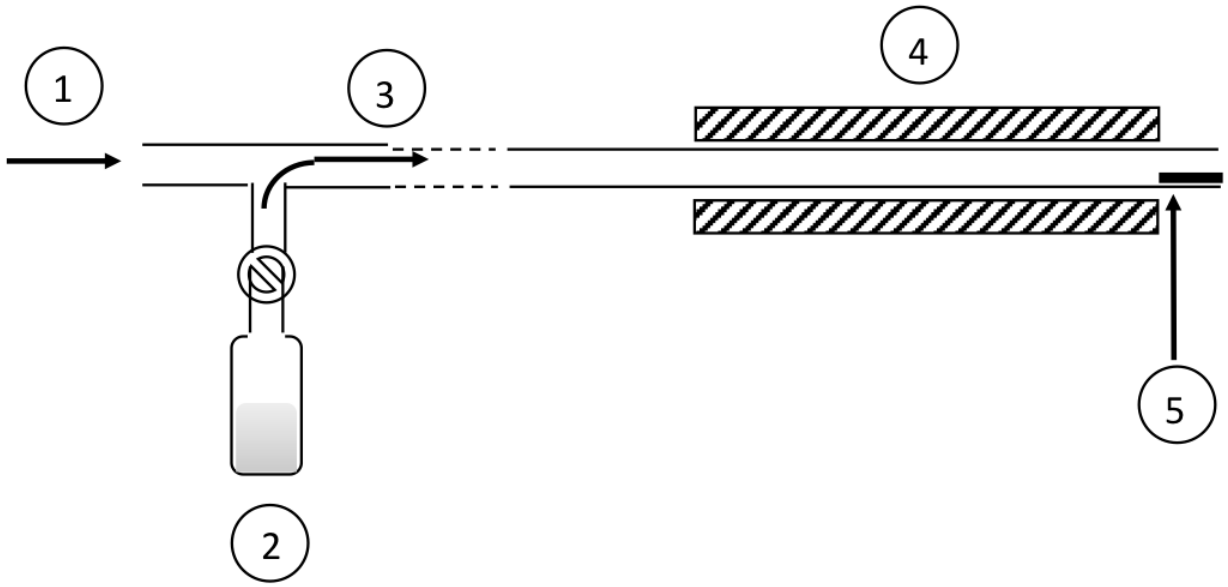
1
3
4
5
2

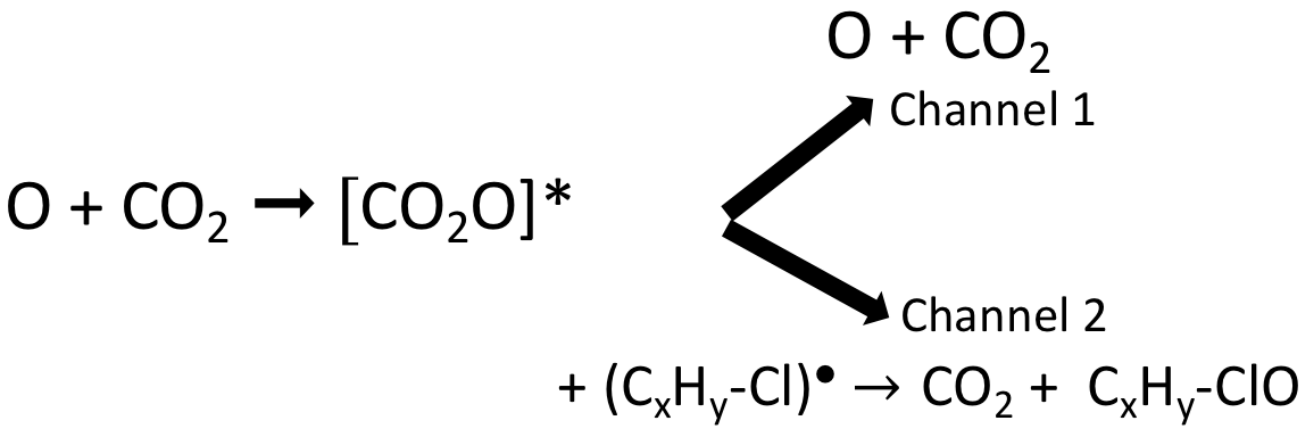
O + CO2
Channel 1
O + CO2 → [CO2O]*
Channel 2
+ (CxHy-Cl)• → CO2 + CxHy-ClO

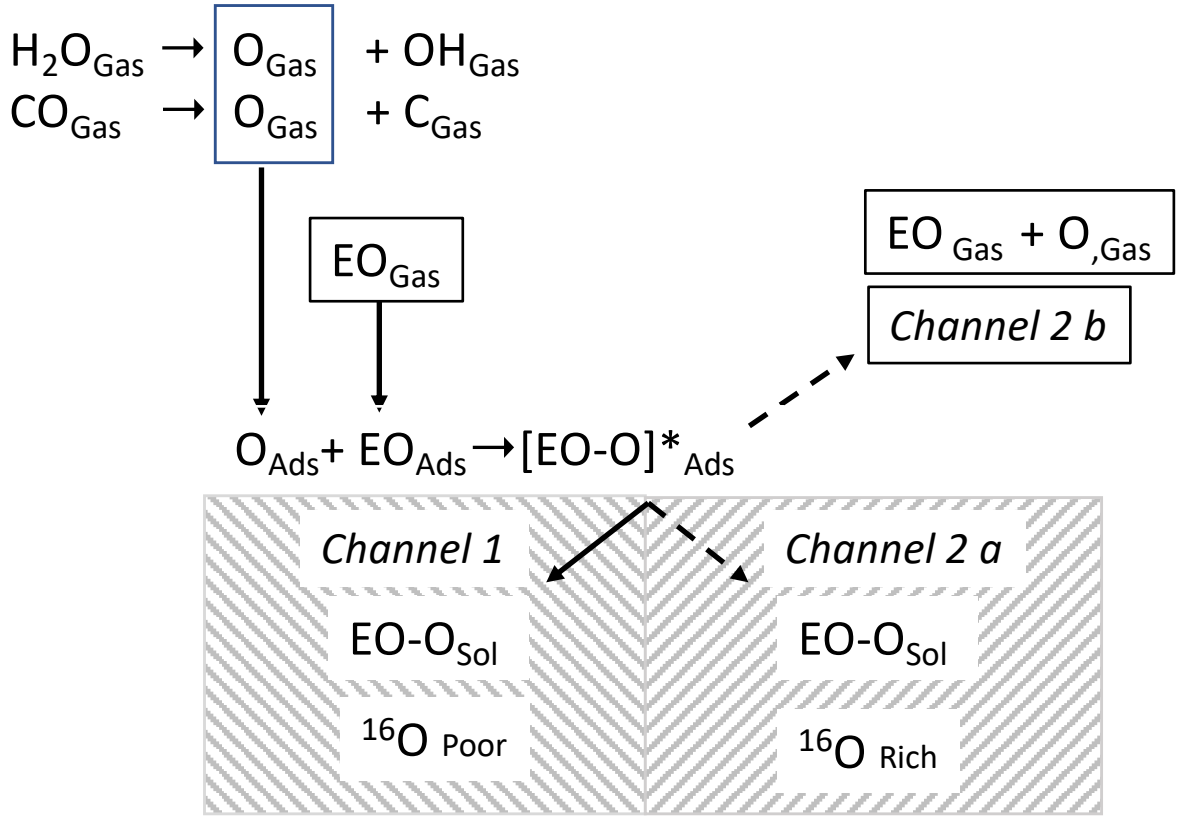
H_2O_{Gas} → O_{Gas} + OH_{Gas}
CO_{Gas} → O_{Gas} + C_{Gas}
EO_{Gas}
EO_{Gas} + $O_{,Gas}$
Channel 2 b
O_{Ads}+ EO_{Ads} → $[EO-O]^*_{Ads}$
Channel 1
Channel 2 a
EO-O_{Sol}
EO-O_{Sol}
^{16}O Poor
^{16}O Rich

PNAS
www.pnas.org

Oxygen and Magnesium Mass Independent Isotopic Fractionation Induced by Chemical Reactions in Plasma

Supplementary Materials

François Robert [*, 1], Marc Chaussidon[2], Adriana Gonzalez-Cano[2], Smail Mostefaoui[1]

(1) Institut Origine et Evolution (O&E), Muséum national d'Histoire naturelle, Sorbonne Université, IMPMC-UMR 7590 CNRS, 57 rue Cuvier 75005 Paris, France.

(2) Université de Paris, Institut de physique du globe de Paris, CNRS, F-75005 Paris, France.

*François ROBERT

Email: (*) : francois.robert@mnhn.fr

S1: MIF effects in different experiments.

E	Chemical compounds	Inorganic E	Organic E (hetero-element)	Chemical reactant	Grains[3]	Hotspots[4]	MIF
Mg	Magnesium dichloride in Pentanol	$MgCl_2$	---	$C_5H_{11}OH$ / N_2	Yes	Yes	Yes
Mg	Methylmagnesium chloride in THF[1]	---	CH_3MgCl	N_2	No	No	No
Mg	Methylmagnesium chloride in THF[1]	N_2O	CH_3MgCl	---	No	No	No
O	Pentanol	N_2O	---	$C_5H_{11}OH$	No	No	Yes
O	Triacetoxy(vinyl)silane[2]	---	$(CH_3CO_2)_3$ SiCH - CH_2	N_2	No	No	No
O	Triacetoxy(vinyl)silane[2]	N_2O	$(CH_3CO_2)_3$ SiCH - CH_2	---	No	No	No
O	Magnesium dichloride in Pentanol	N_2O	---	$MgCl_2$ / $C_5H_{11}OH$	Yes	Yes	No
O	Magnesium dichloride in Pentanol	CO_2	---	$MgCl_2$ / $C_5H_{11}OH$	Yes	Yes	Yes

Notes: (1) Tetrahydrofuran. (2) Si has 3 oxygen bonds. (3) Optical grains on the silicon wafer (4) hospots designate an increase in the ionic intensity i.e. in a change in the ionic emissivity caused by a different chemical speciation of oxygen. These hotpots are revealed by the ion imaging mode of the NanoSims.

Table S1: The first column designates the element E (Mg or O) for which the isotopic compositions have been measured. In the last 3 columns, "*Yes*" indicates that grains (optical microscopy), hospots (NanoSims) or MIF were observed. No MIF effect was detected for Mg when using an organic bonded Mg-Cl instead of $MgCl_2$ in solution with Pentanol. MIF effects on O were observed for Pentanol or Pentanol/$MgCl_2$ in presence of N_2O and CO_2, respectively but not with Pentanol/$MgCl_2$ in presence of N_2O. No MIF effect was detected for O when using organic bonded O atoms. Optical grains are not systematically associated with MIF effects.

S2. NanoSims analytical protocols

	Magnesium	**Oxygen**	**Oxygen**
Session	March 2020	Nov. 2018	July 2020
Primary current	O^-	Cs^+	Cs^+
Beam Current (pA)	13	650	1.8
Diameter Aperture	D1-2	D1-1	D1-3
Presputtering time (min)	5	2	5
Presputtering current (pA)	2000	1500	180
Secondary currents	Mg+	O^-	O^-
Eletron multipliers	$^{24,25,26}Mg^+$	$^{17,18}O^-$	$^{16,17,18}O^-$
Faraday cup		$^{16}O^-$	
Rastering	20x20 μm	No Image	20x20 μm
Pixels	256 x 256	-----	256 x 256
Dwell time (ms/pixel)	1000	-----	1000
Mass resolution	8000	8500	8000
Entrance slit	ES3	ES3	ES3
Aperure slit	AS2	AS3	AS2
Dead Time	44 ns	44 ns	44 ns
Reference for δ units	PDCM	PDCM	PDCM

Table S2: The instrumental parameters of the NanoSIMS.

S3.1

EM on 24Mg, 25Mg and 26Mg MgCl2 in Pentanol / N2				25Mg/24Mg Reference Std value	1.234E-01							
				26Mg/24Mg Reference Std value	1.371E-01							
	Sample	Comments		24Mg Tot.	24Mg cps	25Mg Tot.	25Mg cps	26Mg Tot.	26Mg cps	Delta 26Mg ‰	± (2 std.dev) ‰	Delta 25Mg ‰	± (2 std.dev) ‰
Olivine San Carlos. Used as a standard : Delta 17, 18 = 0 ‰													
Rastering (2x2)	sple@1_1	Polished Sample	Randoom Area 1	1.15E+07	1.12E+05	1.43E+06	1.40E+04	1.57E+06	1.54E+04	-2.3	1.6	8.9	1.7
Rastering (2x2)	sple@1_2	Polished Sample	Randoom Area 2	1.07E+07	1.05E+05	1.34E+06	1.31E+04	1.47E+06	1.43E+04	-4.5	1.7	8.8	1.7
Rastering (2x2)	sple@1_3	Polished Sample	Randoom Area 3	1.10E+07	1.08E+05	1.37E+06	1.34E+04	1.51E+06	1.47E+04	-2.9	1.6	8.8	1.7
Rastering (2x2)	sple@1_4	Polished Sample	Randoom Area 4	1.11E+07	1.09E+05	1.39E+06	1.35E+04	1.52E+06	1.48E+04	-4.5	1.6	9.8	1.7
Rastering (2x2)	sple@1_5	Polished Sample	Randoom Area 5	1.11E+07	1.08E+05	1.37E+06	1.34E+04	1.51E+06	1.47E+04	-6.8	1.6	7.5	1.7
Rastering (2x2)	sple@1_6	Polished Sample	Randoom Area 6	1.08E+07	1.06E+05	1.35E+06	1.32E+04	1.48E+06	1.44E+04	-3.6	1.6	10.6	1.7
Rastering (2x2)	sple@1_7	Polished Sample	Randoom Area 7	1.11E+07	1.09E+05	1.38E+06	1.35E+04	1.52E+06	1.48E+04	-3.9	1.6	8.7	1.7
Rastering (2x2)	sple@1_8	Polished Sample	Randoom Area 8	1.12E+07	1.10E+05	1.40E+06	1.36E+04	1.53E+06	1.49E+04	-7.7	1.6	5.9	1.7
Rastering (2x2)	sple@1_9	Polished Sample	Randoom Area 9	1.09E+07	1.06E+05	1.35E+06	1.32E+04	1.47E+06	1.44E+04	-9.3	1.6	8.4	1.7
Rastering (2x2)	sple@1_10	Polished Sample	Randoom Area 10	1.12E+07	1.09E+05	1.39E+06	1.35E+04	1.52E+06	1.48E+04	-8.6	1.6	5.3	1.7
Rastering (2x2)	Robert-Juillet-2019_1	Polished Sample	Randoom Area 1	2.22E+06	1.11E+04	2.81E+05	1.40E+03	3.13E+05	1.56E+03	27.4	3.6	25.1	3.8
Rastering (2x2)	Robert-Juillet-2019_2	Polished Sample	Randoom Area 2	2.26E+06	1.13E+04	2.86E+05	1.43E+03	3.16E+05	1.58E+03	19.8	3.6	24.3	3.7
Rastering (2x2)	Robert-Juillet-2019_3	Polished Sample	Randoom Area 3	6.61E+06	3.30E+04	8.21E+05	4.11E+03	9.00E+05	4.50E+03	-6.2	2.1	7.4	2.2
Rastering (2x2)	Robert-Juillet-2019_4	Polished Sample	Randoom Area 4	6.26E+06	3.13E+04	7.78E+05	3.89E+03	8.51E+05	4.25E+03	-9.4	2.2	7.1	2.3
PDCM (used as a standard) FR20	Sample			24Mg cps	25Mg cps	26Mg cps	24Mg Tot.	25Mg Tot.	26Mg Tot.	Delta 26Mg ‰	± (2 std.dev) ‰	Delta 25Mg ‰	± (2 std.dev) ‰
Rastering (25x25)	Robert-April-2019_3.im	Hot-Spot 1 in Powder	Image 3	1.11E+04	1.37E+03	1.53E+03	3.32E+05	4.10E+04	4.57E+04	6.0	9.4	2.9	9.9
Rastering (25x25)	Robert-April-2019_4.im	Hot-Spot 1 in Powder	Image 4	4.55E+04	5.60E+03	6.16E+03	7.42E+05	9.14E+04	1.01E+05	-11.3	6.3	-1.8	6.6
Rastering (25x25)	Robert-April-2019_4.im	Hot-Spot 2 in Powder	Image 4	3.61E+04	4.50E+03	4.94E+03	3.07E+05	3.83E+04	4.20E+04	-1.5	9.8	11.4	10.2
Rastering (25x25)	Robert-April-2019_4.im	Hot-Spot 3 in Powder	Image 4	3.20E+04	3.97E+03	4.41E+03	2.80E+05	3.47E+04	3.85E+04	4.7	10.2	5.7	10.7
Rastering (25x25)	Robert-April-2019_4.im	Hot-Spot 4 in Powder	Image 4	2.54E+04	3.16E+03	3.44E+03	1.83E+05	2.27E+04	2.47E+04	-13.6	12.7	7.3	13.3
Rastering (25x25)	Robert-April-2019_4.im	Hot-Spot 5 in Powder	Image 4	1.55E+04	1.92E+03	2.11E+03	1.67E+05	2.08E+04	2.28E+04	-4.9	13.2	7.3	13.9
Rastering (25x25)	Robert-April-2019_5_mod.im	Hot-Spot 1 in Powder	Image 5	1.13E+05	1.40E+04	1.54E+04	1.78E+06	2.19E+05	2.41E+05	-12.5	4.1	-2.0	4.3
Rastering (25x25)	Robert-April-2019_6.im	Hot-Spot 1 in Powder	Image 6	1.13E+05	1.40E+04	1.54E+04	1.87E+06	2.31E+05	2.54E+05	-8.0	4.0	1.2	4.2
Rastering (25x25)	Robert-April-2019_6.im	Hot-Spot 2 in Powder	Image 6	6.98E+04	8.56E+03	9.50E+03	4.85E+05	5.95E+04	6.60E+04	-7.4	7.8	-6.3	8.2
Rastering (25x25)	Robert-April-2019_6.im	Hot-Spot 3 in Powder	Image 6	8.04E+04	9.87E+03	1.08E+04	1.51E+06	1.86E+05	2.03E+05	-21.2	4.4	-4.6	4.6
Rastering (25x25)	Robert-April-2019_7_mod.im	Hot-Spot 1 in Powder	Image 7	7.09E+04	8.70E+03	9.63E+03	1.99E+06	2.44E+05	2.70E+05	-9.8	3.8	-5.4	4.0
Rastering (25x25)	Robert-April-2019_7_mod.im	Hot-Spot 2 in Powder	Image 7	6.85E+04	8.38E+03	9.31E+03	8.59E+05	1.05E+05	1.17E+05	-8.5	5.9	-8.5	6.2
Rastering (25x25)	Robert-April-2019_7_mod.im	Hot-Spot 3 in Powder	Image 7	1.20E+05	1.46E+04	1.61E+04	2.86E+06	3.49E+05	3.84E+05	-21.8	3.2	-12.1	3.4
Rastering (25x25)	Robert-April-2019_7_mod.im	Hot-Spot 7 in Powder	Image 7	8.27E+04	1.01E+04	1.13E+04	1.13E+06	1.38E+05	1.55E+05	-4.1	5.1	-8.7	5.4
Rastering (25x25)	Robert-April-2019_7_mod.im	Hot-Spot 8 in Powder	Image 7	8.88E+04	1.08E+04	1.19E+04	2.32E+06	2.84E+05	3.12E+05	-20.7	3.6	-9.8	3.8
Rastering (25x25)	Robert-April-2019_8.im	Hot-Spot 1 on Si-Wafer	Image 8	6.19E+04	7.52E+03	8.41E+03	1.35E+06	1.64E+05	1.83E+05	-9.4	4.7	-15.9	4.9
Rastering (25x25)	Robert-April-2019_9.im	Hot-Spot 1 on Si-Wafer	Image 9	1.59E+05	1.97E+04	2.21E+04	1.44E+07	1.78E+06	2.00E+06	14.9	1.4	4.0	1.5
Rastering (25x25)	Robert-April-2019_11.im	Hot-Spot 1 on Si-Wafer	Image 11	3.39E+04	4.20E+03	4.64E+03	3.16E+06	3.91E+05	4.33E+05	-1.6	3.0	2.9	3.2
Rastering (25x25)	Robert-April-2019_11.im	Hot-Spot 2 on Si-Wafer	Image 11	1.99E+04	2.47E+03	2.75E+03	2.07E+06	2.56E+05	2.85E+05	5.8	3.7	4.3	3.9
Rastering (25x25)	Robert-April-2019_11.im	Hot-Spot 3 on Si-Wafer	Image 11	1.91E+04	2.38E+03	2.63E+03	2.74E+06	3.42E+05	3.78E+05	6.2	3.3	12.8	3.4
Rastering (25x25)	Robert-April-2019_11.im	Hot-Spot 4 on Si-Wafer	Image 11	8.36E+03	1.03E+03	1.13E+03	1.77E+05	2.18E+04	2.39E+04	-13.1	12.9	1.3	13.5

Table S3.1: Magnesium isotopic composition expressed as δ^{25}Mg(‰) and δ^{26}Mg(‰).The ionic counting rates are expressed in counts per second (cps) while the total number of counts (Tot) depend on the duration of the measurement. The average value of the PDCM is used as the *Reference Std. value* for calculating the δ values of the hotspots exhibiting marked departure in their isotopic composition. The ionic ratios ^{25}Mg/^{24}Mg and ^{26}Mg/^{24}Mg used to calculate the δ values are indicated as *Reference Std value*. Error bars are the statistical precision calculated on the total number of counts ($\pm 2\sigma$). Two examples of the statistical distribution of the data is shown for (1) an olivine sample (San Carlos) and (2) 1 region of the sample obtained in the $MgCl_2$ - Pentanol - N_2 experiment (noted PDCM) showing a statistical distribution of isotope ratios. The PDCM isotopic distribution is reported in Figure S3.1 bellow.

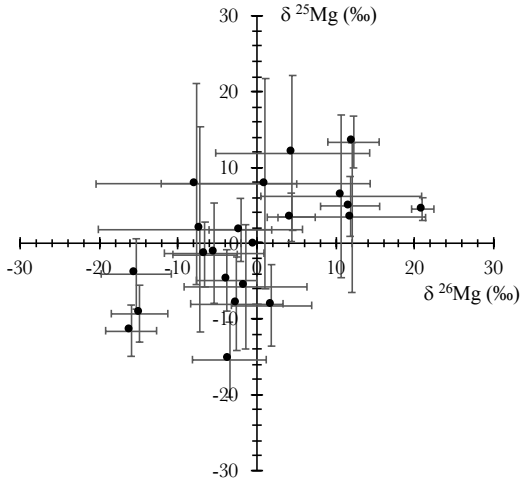

Figure S3.1: An example of the distribution of data recorded randomly on the PDCM is shown as δ^{25}Mg (‰) *vs.* δ^{26}Mg (‰). The reproducibility on this set of data is 15.6 and ±19.8 (2σ) for δ^{25}Mg (‰) and δ^{26}Mg (‰), respectively. Error bars stand for the statistical analytical error.

Table S3.2:

25Mg/24Mg PDCM used as a reference 1.234E-01
26Mg/24Mg PDCM used as a reference 1.371E-01

Sample FR20 - Individual grain on upstream Si Wafer		Comments		24Mg Tot.	24Mg cps	25Mg Tot.	25Mg cps	26Mg Tot.	26Mg cps	Delta 26 ‰	2 sigma ±	Delta 25 ‰	2 sigma ±
Rastering (25x25)	Robert-Juillet-2019_21.im	Surface - 2D	Image 21	6.47E+06	9.54E+02	7.25E+05	1.07E+02	8.14E+05	1.20E+02	-83.3	2.3	-92.5	2.2
Rastering (25x25)	Robert-Juillet-2019_21.im	Surface to core 2D	Image 21	8.56E+06	5.42E+04	1.08E+06	6.83E+03	1.18E+06	7.46E+03	3.1	1.9	21.5	1.8
Rastering (25x25)	Robert-Juillet-2019_21.im	Surface to core 2D	Image 21	1.27E+07	1.28E+05	1.60E+06	1.60E+04	1.74E+06	1.74E+04	-4.3	1.6	18.3	1.5
Rastering (25x25)	Robert-Juillet-2019_21.im	Surface to core 2D	Image 21	1.16E+07	2.26E+05	1.46E+06	2.84E+04	1.58E+06	3.08E+04	-6.4	1.7	19.8	1.6
Rastering (25x25)	Robert-Juillet-2019_21.im	Surface to core 2D	Image 21	1.81E+07	3.22E+05	2.27E+06	4.05E+04	2.46E+06	4.40E+04	-5.7	1.3	17.6	1.3
Rastering (25x25)	Robert-Juillet-2019_21.im	Surface to core 2D	Image 21	8.78E+06	3.82E+05	1.10E+06	4.80E+04	1.20E+06	5.21E+04	-5.6	1.9	19.4	1.8
Rastering (25x25)	Robert-Juillet-2019_21.im	Core -2D	Image 21	6.66E+07	9.25E+03	8.29E+06	1.15E+03	9.03E+06	1.25E+03	-11.6	0.7	8.4	0.7
Rastering (25x25)	Robert-Juillet-2019_21.im	Surface - 3D	Image 21	2.20E+06	3.54E+03	2.65E+05	4.27E+02	2.93E+05	4.71E+02	-30.2	3.7	-23.2	3.9
Rastering (25x25)	Robert-Juillet-2019_21.im	From Surface to Depth -3D	Image 21	1.50E+06	2.41E+03	1.81E+05	2.91E+02	2.02E+05	3.24E+02	-20.1	4.5	-23.5	4.7
Rastering (25x25)	Robert-Juillet-2019_21.im	From Surface to Depth- 3D	Image 21	1.25E+06	2.02E+03	1.49E+05	2.39E+02	1.67E+05	2.68E+02	-30.1	4.9	-37.8	5.2
Rastering (25x25)	Robert-Juillet-2019_21.im	From Surface to Depth- 3D	Image 21	6.70E+05	1.08E+03	7.61E+04	1.22E+02	8.55E+04	1.38E+02	-68.3	6.8	-79.4	7.3
Rastering (25x25)	Robert-Juillet-2019_21.im	From Surface to Depth- 3D	Image 21	5.23E+05	8.40E+02	5.72E+04	9.20E+01	6.45E+04	1.04E+02	-99.8	7.9	-112.5	8.4
Rastering (25x25)	Robert-Juillet-2019_21.im	From Surface to Depth- 3D	Image 21	3.41E+05	5.49E+02	3.47E+04	5.58E+01	4.01E+04	6.45E+01	-142.9	10.0	-175.3	10.7
Rastering (25x25)	Robert-Juillet-2019_21.im	From Surface to Depth- 3D	Image 21	3.36E+05	5.40E+02	3.47E+04	5.58E+01	3.91E+04	6.29E+01	-150.7	10.1	-162.6	10.7
Rastering (25x25)	Robert-Juillet-2019_21.im	From Surface to Depth- 3D	Image 21	2.81E+05	4.52E+02	2.78E+04	4.46E+01	3.21E+04	5.15E+01	-167.7	11.2	-198.7	12.0
Rastering (25x25)	Robert-Juillet-2019_21.im	From Surface to Depth- 3D	Image 21	3.11E+05	4.99E+02	3.19E+04	5.13E+01	3.58E+04	5.75E+01	-160.5	10.6	-166.5	11.2
Rastering (25x25)	Robert-Juillet-2019_21.im	From Surface to Depth- 3D	Image 21	2.44E+05	3.92E+02	2.42E+04	3.89E+01	2.74E+04	4.40E+01	-181.1	12.1	-195.9	12.9
Rastering (25x25)	Robert-Juillet-2019_21.im	Depth - 3D	Image 21	2.40E+05	3.86E+02	2.39E+04	3.84E+01	2.69E+04	4.32E+01	-184.2	12.2	-194.4	12.9
Rastering (25x25)	Robert-Juillet-2019_23.im	Surface - 2D	Image 23	1.83E+06	2.67E+02	1.97E+05	2.89E+01	2.08E+05	3.04E+01	-170.4	4.4	-123.8	4.5
Rastering (25x25)	Robert-Juillet-2019_23.im	Surface to core - 2D	Image 23	4.55E+06	2.12E+04	5.74E+05	2.68E+03	6.26E+05	2.93E+03	4.0	2.5	22.0	2.6
Rastering (25x25)	Robert-Juillet-2019_23.im	Surface to core - 2D	Image 23	1.13E+07	1.08E+05	1.41E+06	1.36E+04	1.54E+06	1.48E+04	-6.4	1.6	15.5	1.7
Rastering (25x25)	Robert-Juillet-2019_23.im	Surface to core - 2D	Image 23	8.63E+06	2.21E+05	1.08E+06	2.76E+04	1.17E+06	2.99E+04	-11.7	1.8	13.5	1.9
Rastering (25x25)	Robert-Juillet-2019_23.im	Surface to core - 2D	Image 23	4.66E+06	2.82E+05	5.84E+05	3.54E+04	6.32E+05	3.83E+04	-10.4	2.5	15.0	2.6
Rastering (25x25)	Robert-Juillet-2019_23.im	Surface to core - 2D	Image 23	3.11E+07	4.32E+03	3.87E+06	5.37E+02	4.20E+06	5.82E+02	-16.6	1.0	7.6	1.0
Rastering (25x25)	Robert-Juillet-2019_23.im	Bulk - 2D	Image 23	2.66E+07	1.29E+05	3.33E+06	1.61E+04	3.62E+06	1.75E+04	-8.4	1.1	14.9	1.1
Rastering (25x25)	Robert-Juillet-2019_23.im	Surface - 3D	Image 23	7.53E+05	1.21E+03	8.15E+04	1.31E+02	8.96E+04	1.44E+02	-131.6	7.0	-122.5	6.7
Rastering (25x25)	Robert-Juillet-2019_23.im	From Surface to Depth - 3D	Image 23	4.58E+05	7.37E+02	4.48E+04	7.21E+01	5.00E+04	8.05E+01	-203.6	9.4	-207.0	8.9
Rastering (25x25)	Robert-Juillet-2019_23.im	From Surface to Depth - 3D	Image 23	2.79E+05	4.49E+02	2.70E+04	4.35E+01	3.05E+04	4.91E+01	-202.6	12.2	-214.8	11.5
Rastering (25x25)	Robert-Juillet-2019_23.im	From Surface to Depth - 3D	Image 23	1.36E+05	2.18E+02	1.14E+04	1.83E+01	1.26E+04	2.03E+01	-321.7	18.8	-320.2	17.8
Rastering (25x25)	Robert-Juillet-2019_23.im	From Surface to Depth - 3D	Image 23	8.98E+04	1.45E+02	1.36E+04	2.19E+01	8.87E+03	1.43E+01	-280.2	17.1	227.5	21.2
Rastering (25x25)	Robert-Juillet-2019_23.im	From Surface to Depth - 3D	Image 23	4.72E+04	7.60E+01	7.80E+03	1.26E+01	3.66E+03	5.89E+00	-435.5	22.6	339.0	33.1
Rastering (25x25)	Robert-Juillet-2019_23.im	From Surface to Depth - 3D	Image 23	3.15E+04	5.07E+01	5.45E+03	8.77E+00	6.04E+03	9.73E+00	398.9	27.1	401.3	25.7
Rastering (25x25)	Robert-Juillet-2019_23.im	From Surface to Depth - 3D	Image 23	1.12E+04	1.81E+01	2.62E+03	4.22E+00	2.93E+03	4.71E+00	903.9	39.1	893.5	37.0
Rastering (25x25)	Robert-Juillet-2019_23.im	From Surface to Depth - 3D	Image 23	5.06E+03	8.14E+00	1.14E+03	1.84E+00	1.27E+03	2.04E+00	823.6	59.2	828.2	56.2
Rastering (25x25)	Robert-Juillet-2019_23.im	At Depth - 3D	Image 23	4.82E+03	7.76E+00	6.49E+02	1.04E+00	6.94E+02	1.12E+00	50.5	78.5	91.9	75.9
Rastering (25x25)	Robert-Juillet-2019_23.im	Beneath the grain - 3D	Image 23	5.46E+04	4.49E+00	7.00E+03	5.76E-01	7.26E+03	5.98E-01	-29.3	23.5	40.0	23.9

Table S3.2: Magnesium isotopic composition expressed as δ^{25}Mg(‰) and δ^{26}Mg(‰). The plasma discharge is generated in a mixture $MgCl_2$ - Pentanol - N_2. The ionic counting rates are expressed in counts per second (cps) while the total number of counts (Tot) depend on the duration of the measurement. Error bars are the statistical precision calculated on the total number of counts (±2σ). The average value of the PDCM is used as the reference value (cf. previous Table S3.1) for calculating the δ values of the hotspots exhibiting marked departure in their isotopic composition. The average PDCM ionic ratios $^{25}Mg/^{24}Mg$ and $^{26}Mg/^{24}Mg$ are indicated as *Reference Std value*. Samples noted 2D and 3D indicates that the Mg isotopic compositions were measured (i) by image analysis as a cross section from the surface to the core of the hotspots (ii) by depth profiling until the complete disappearance of the hotspot caused by its sputtering. This Table was used to construct the Figure 1 of the text.

S3.3

Faraday on 16O, EM on 17O and 18O
Pentanol / N2O

17O/16O Reference value for delta 3.709E-04
18O/16O Reference value for delta 1.972E-03

San Carlos Olivine.	Sample	Comments	16O Tot.	16O Cps	17O Tot.	17O Cps	18O Tot.	18O Cps	Delta 18 ‰	± 18 (2s) ‰	Delta 17 ‰	±17 (2s) ‰
Randoom Area 1	Robert-Oct-2019_1.im	Polished section	9.52E+07	1.16E+05	3.70E+04	4.52E+01	1.97E+05	2.41E+02	49.9	4.5	48.8	10.4
Randoom Area 3	Robert-Oct-2019_1.im	Polished section	8.41E+07	1.03E+05	3.30E+04	4.03E+01	1.74E+05	2.13E+02	51.1	4.8	57.9	11.0
Randoom Area 1	Robert-Oct-2019_2.im	Polished section	1.39E+08	1.05E+05	5.40E+04	4.05E+01	2.87E+05	2.16E+02	48.6	3.7	46.7	8.6
Randoom Area 2	Robert-Oct-2019_2.im	Polished section	1.15E+08	8.66E+04	4.52E+04	3.39E+01	2.37E+05	1.78E+02	47.3	4.1	58.5	9.4
Randoom Area 3	Robert-Oct-2019_2.im	Polished section	1.39E+08	1.04E+05	5.43E+04	4.08E+01	2.87E+05	2.16E+02	47.3	3.7	53.2	8.6
Randoom Area 4	Robert-Oct-2019_2.im	Polished section	1.32E+08	9.91E+04	5.18E+04	3.89E+01	2.74E+05	2.06E+02	52.9	3.8	57.5	8.8

D. Rumble's Kerogen	Sample	Comments	16O Tot.	16O Cps	17O Tot.	17O Cps	18O Tot.	18O Cps	Delta 18 ‰	± 18 (2s) ‰	Delta 17 ‰	±17 (2s) ‰
Randoom Area 1	Robert-Oct-2019_5.im	Organic Matter in Powder	2.20E+08	6.25E+04	8.62E+04	2.44E+01	4.55E+05	1.29E+02	48.0	6.8	56.4	3.0
Randoom Area 2	Robert-Oct-2019_5.im	Organic Matter in Powder	1.83E+08	5.17E+04	7.14E+04	2.02E+01	3.77E+05	1.07E+02	45.7	7.5	51.4	3.3
Randoom Area 3	Robert-Oct-2019_5.im	Organic Matter in Powder	2.40E+07	6.80E+03	9.32E+03	2.64E+00	4.88E+04	1.38E+01	32.2	20.7	46.8	9.0
Randoom Area 4	Robert-Oct-2019_5.im	Organic Matter in Powder	3.10E+08	8.80E+04	1.21E+05	3.43E+01	6.33E+05	1.79E+02	35.0	5.7	53.8	2.5
Randoom Area 5	Robert-Oct-2019_5.im	Organic Matter in Powder	1.47E+08	4.16E+04	5.76E+04	1.63E+01	3.03E+05	8.58E+01	43.9	8.3	56.3	3.6
Randoom Area 6	Robert-Oct-2019_5.im	Organic Matter in Powder	1.27E+08	3.61E+04	4.95E+04	1.40E+01	2.62E+05	7.44E+01	48.1	9.0	50.3	3.9
Randoom Area 7	Robert-Oct-2019_5.im	Organic Matter in Powder	2.30E+08	6.53E+04	9.02E+04	2.56E+01	4.75E+05	1.35E+02	47.3	6.7	57.5	2.9
Randoom Area 8	Robert-Oct-2019_5.im	Organic Matter in Powder	3.30E+07	9.34E+03	1.29E+04	3.65E+00	6.77E+04	1.92E+01	40.4	17.6	51.3	7.7
Randoom Area 9	Robert-Oct-2019_5.im	Organic Matter in Powder	1.80E+07	5.11E+03	7.04E+03	1.99E+00	3.69E+04	1.05E+01	40.9	23.8	53.9	10.4

FR9 PDCM (Used as Reference)	Sample	Comments	16O Tot.	16O Cps	17O Tot.	17O Cps	18O Tot.	18O Cps	Delta 18 ‰	± 18 (2s) ‰	Delta 17 ‰	±17 (2s) ‰
Rastering (15x15)	FR9@1_1	Collected as a Powder	7.65E+08	2.34E+06	2.86E+05	8.72E+02	1.52E+06	4.65E+03	9.8	1.6	6.4	3.7
Rastering (15x15)	FR9@1_2	Collected as a Powder	8.01E+08	2.44E+06	2.95E+05	8.99E+02	1.58E+06	4.82E+03	0.5	1.6	-7.9	3.7
Rastering (15x15)	FR9@1_3	Collected as a Powder	7.78E+08	2.37E+06	2.89E+05	8.82E+02	1.53E+06	4.67E+03	-2.7	1.6	2.2	3.7
Rastering (15x15)	FR9@1_4	Collected as a Powder	8.18E+08	2.50E+06	3.06E+05	9.32E+02	1.60E+06	4.89E+03	-5.9	1.6	6.6	3.6
Rastering (15x15)	FR9@1_5	Collected as a Powder	7.47E+08	2.28E+06	2.80E+05	8.54E+02	1.51E+06	4.59E+03	22.7	1.6	10.2	3.8
Rastering (15x15)	FR9@1_6	Collected as a Powder	7.87E+08	2.40E+06	2.92E+05	8.92E+02	1.57E+06	4.80E+03	12.9	1.6	0.4	3.7
Rastering (15x15)	FR9@1_7	Collected as a Powder	7.66E+08	2.34E+06	2.83E+05	8.63E+02	1.54E+06	4.70E+03	20.5	1.6	-4.7	3.8
Rastering (15x15)	FR9@1_8	Collected as a Powder	8.77E+08	2.68E+06	3.20E+05	9.76E+02	1.71E+06	5.23E+03	-8.9	1.5	-16.3	3.5
Rastering (15x15)	FR9@1_9	Collected as a Powder	7.95E+08	2.43E+06	2.99E+05	9.12E+02	1.56E+06	4.75E+03	-7.1	1.6	14.1	3.7
Rastering (15x15)	FR9@1_10	Collected as a Powder	8.16E+08	2.49E+06	3.04E+05	9.26E+02	1.63E+06	4.97E+03	11.5	1.6	3.0	3.6
Rastering (15x15)	FR9@1_11	Collected as a Powder	8.13E+08	2.48E+06	3.05E+05	9.30E+02	1.64E+06	5.00E+03	21.9	1.6	10.7	3.6
Rastering (15x15)	FR9@1_12	Collected as a Powder	8.33E+08	2.54E+06	3.05E+05	9.32E+02	1.65E+06	5.03E+03	2.8	1.6	-12.3	3.6
Rastering (15x15)	FR9@1_13	Collected as a Powder	8.73E+08	2.66E+06	3.21E+05	9.79E+02	1.72E+06	5.24E+03	-2.5	1.5	-9.3	3.5
Rastering (15x15)	FR9@1_14	Collected as a Powder	7.92E+08	2.42E+06	2.92E+05	8.91E+02	1.55E+06	4.73E+03	-6.4	1.6	-6.3	3.7
Rastering (15x15)	FR9@1_15	Collected as a Powder	8.24E+08	2.52E+06	3.08E+05	9.39E+02	1.62E+06	4.94E+03	-4.7	1.6	6.9	3.6
Rastering (15x15)	FR9@1_16	Collected as a Powder	8.19E+08	2.50E+06	3.04E+05	9.27E+02	1.60E+06	4.89E+03	-8.5	1.6	0.0	3.6
Rastering (15x15)	FR9@1_17	Collected as a Powder	8.33E+08	2.54E+06	3.12E+05	9.51E+02	1.63E+06	4.99E+03	-5.1	1.6	8.4	3.6
Rastering (15x15)	FR9@1_18	Collected as a Powder	8.27E+08	2.52E+06	3.10E+05	9.45E+02	1.62E+06	4.94E+03	-7.3	1.6	9.6	3.6
Rastering (15x15)	FR9@1_19	Collected as a Powder	7.32E+08	2.23E+06	2.75E+05	8.38E+02	1.43E+06	4.35E+03	-11.7	1.7	12.1	3.8
Rastering (15x15)	FR9@1_20	Collected as a Powder	8.87E+08	2.71E+06	3.28E+05	1.00E+03	1.78E+06	5.42E+03	16.6	1.5	-2.7	3.5
Rastering (15x15)	FR9@1_21	Collected as a Powder	7.97E+08	2.43E+06	2.96E+05	9.04E+02	1.59E+06	4.87E+03	14.8	1.6	1.9	3.7
Rastering (15x15)	FR9@1_22	Collected as a Powder	7.78E+08	2.37E+06	2.87E+05	8.75E+02	1.52E+06	4.64E+03	-8.6	1.6	-6.1	3.7
Rastering (15x15)	FR9@1_23	Collected as a Powder	7.87E+08	2.40E+06	2.87E+05	8.77E+02	1.55E+06	4.72E+03	-3.7	1.6	-15.9	3.7
Rastering (15x15)	FR9@1_24	Collected as a Powder	7.94E+08	2.42E+06	2.92E+05	8.90E+02	1.56E+06	4.75E+03	-5.0	1.6	-9.6	3.7
Rastering (15x15)	FR9@1_25	Collected as a Powder	7.77E+08	2.37E+06	2.93E+05	8.93E+02	1.53E+06	4.67E+03	-0.6	1.6	15.6	3.7
Rastering (15x15)	FR9@1_26	Collected as a Powder	8.33E+08	2.54E+06	3.12E+05	9.51E+02	1.66E+06	5.07E+03	12.0	1.6	8.8	3.6
Rastering (15x15)	FR9@1_27	Collected as a Powder	8.27E+08	2.52E+06	3.08E+05	9.39E+02	1.64E+06	5.01E+03	7.5	1.6	3.0	3.6
Rastering (15x15)	FR9@1_28	Collected as a Powder	7.71E+08	2.35E+06	2.81E+05	8.58E+02	1.52E+06	4.64E+03	-0.9	1.6	-17.2	3.8
Rastering (15x15)	FR9@1_29	Collected as a Powder	8.27E+08	2.53E+06	3.10E+05	9.46E+02	1.65E+06	5.03E+03	10.9	1.6	9.8	3.6
Rastering (15x15)	FR9@1_30	Collected as a Powder	8.18E+08	2.50E+06	3.03E+05	9.25E+02	1.64E+06	5.01E+03	18.4	1.6	-0.4	3.6
Rastering (15x15)	FR9@1_31	Collected as a Powder	8.16E+08	2.49E+06	2.99E+05	9.13E+02	1.63E+06	4.98E+03	15.5	1.6	-11.0	3.7
Rastering (15x15)	FR9@1_32	Collected as a Powder	8.16E+08	2.49E+06	3.04E+05	9.27E+02	1.63E+06	4.97E+03	11.8	1.6	3.2	3.6
Rastering (15x15)	FR9@1_33	Collected as a Powder	7.81E+08	2.38E+06	2.93E+05	8.95E+02	1.54E+06	4.70E+03	-0.3	1.6	11.8	3.7
Rastering (15x15)	FR9@1_34	Collected as a Powder	8.40E+08	2.56E+06	3.10E+05	9.46E+02	1.65E+06	5.02E+03	-6.1	1.6	-4.9	3.6
Rastering (15x15)	FR9@1_35	Collected as a Powder	8.61E+08	2.63E+06	3.12E+05	9.52E+02	1.68E+06	5.14E+03	-8.5	1.5	-23.2	3.6
Rastering (15x15)	FR9@1_36	Collected as a Powder	7.86E+08	2.40E+06	2.93E+05	8.94E+02	1.54E+06	4.71E+03	-4.5	1.6	5.1	3.7
Rastering (15x15)	FR9@1_37	Collected as a Powder	8.03E+08	2.45E+06	3.00E+05	9.16E+02	1.58E+06	4.81E+03	-5.5	1.6	7.7	3.6
Rastering (15x15)	FR9@1_38	Collected as a Powder	7.96E+08	2.43E+06	2.98E+05	9.11E+02	1.56E+06	4.77E+03	-4.6	1.6	10.5	3.7
Rastering (15x15)	FR9@1_39	Collected as a Powder	7.99E+08	2.44E+06	2.95E+05	9.01E+02	1.56E+06	4.77E+03	-6.6	1.6	-3.8	3.7
Rastering (15x15)	FR9@1_40	Collected as a Powder	8.00E+08	2.44E+06	2.90E+05	8.84E+02	1.56E+06	4.75E+03	-13.0	1.6	-24.3	3.7
Rastering (15x15)	FR9@1_41	Collected as a Powder	7.53E+08	2.30E+06	2.81E+05	8.56E+02	1.46E+06	4.45E+03	-18.2	1.7	4.3	3.8
Rastering (15x15)	FR9@1_42	Collected as a Powder	7.79E+08	2.38E+06	2.90E+05	8.87E+02	1.52E+06	4.63E+03	-11.3	1.6	5.4	3.7
Rastering (15x15)	FR9@1_43	Collected as a Powder	7.58E+08	2.31E+06	2.81E+05	8.59E+02	1.48E+06	4.50E+03	-12.8	1.6	0.8	3.8
Rastering (15x15)	FR9@1_44	Collected as a Powder	7.92E+08	2.42E+06	2.95E+05	9.00E+02	1.54E+06	4.69E+03	-16.0	1.6	3.6	3.7
Rastering (15x15)	FR9@1_45	Collected as a Powder	7.85E+08	2.40E+06	2.92E+05	8.90E+02	1.53E+06	4.66E+03	-14.3	1.6	1.4	3.7
Rastering (15x15)	FR9@1_46	Collected as a Powder	7.62E+08	2.32E+06	2.85E+05	8.70E+02	1.49E+06	4.54E+03	-10.2	1.6	8.5	3.7
Rastering (15x15)	FR9@1_47	Collected as a Powder	7.44E+08	2.27E+06	2.75E+05	8.39E+02	1.45E+06	4.42E+03	-13.4	1.7	-4.5	3.8
Rastering (15x15)	FR9@1_48	Collected as a Powder	8.03E+08	2.45E+06	2.98E+05	9.09E+02	1.56E+06	4.77E+03	-12.3	1.6	0.2	3.7
Rastering (15x15)	FR9@1_49	Collected as a Powder	7.54E+08	2.30E+06	2.78E+05	8.47E+02	1.46E+06	4.45E+03	-19.6	1.7	-6.8	3.8
Rastering (15x15)	FR9@1_50	Collected as a Powder	7.65E+08	2.33E+06	2.84E+05	8.67E+02	1.48E+06	4.51E+03	-19.8	1.6	1.3	3.8
Rastering (15x15)	FR9@1_51	Collected as a Powder	7.39E+08	2.26E+06	2.74E+05	8.37E+02	1.45E+06	4.43E+03	-3.8	1.7	-0.2	3.8
Rastering (15x15)	FR9@1_52	Collected as a Powder	6.88E+08	2.10E+06	2.59E+05	7.90E+02	1.37E+06	4.17E+03	6.5	1.7	13.3	3.9
Rastering (15x15)	FR9@1_53	Collected as a Powder	7.21E+08	2.20E+06	2.64E+05	8.05E+02	1.42E+06	4.35E+03	1.9	1.7	-14.0	3.9
Rastering (15x15)	FR9@1_54	Collected as a Powder	7.17E+08	2.19E+06	2.69E+05	8.20E+02	1.42E+06	4.32E+03	1.8	1.7	10.6	3.9
Rastering (15x15)	FR9@1_55	Collected as a Powder	7.08E+08	2.16E+06	2.61E+05	7.96E+02	1.40E+06	4.26E+03	0.1	1.7	-7.3	3.9
Rastering (15x15)	FR9@1_56	Collected as a Powder	6.97E+08	2.13E+06	2.58E+05	7.89E+02	1.37E+06	4.18E+03	-4.1	1.7	-0.7	3.9
Rastering (15x15)	FR9@1_57	Collected as a Powder	7.36E+08	2.25E+06	2.74E+05	8.36E+02	1.44E+06	4.39E+03	-8.7	1.7	3.2	3.8
Rastering (15x15)	FR9@1_59	Collected as a Powder	7.49E+08	2.29E+06	2.79E+05	8.52E+02	1.47E+06	4.49E+03	-4.5	1.6	5.4	3.8
Rastering (15x15)	FR9@1_60	Collected as a Powder	7.10E+08	2.17E+06	2.60E+05	7.95E+02	1.41E+06	4.29E+03	5.0	1.7	-11.4	3.9
Rastering (15x15)	FR9@1_61	Collected as a Powder	6.46E+08	1.97E+06	2.37E+05	7.24E+02	1.28E+06	3.89E+03	1.3	1.8	-10.8	4.1
Rastering (15x15)	FR9@1_62	Collected as a Powder	6.51E+08	1.99E+06	2.45E+05	7.48E+02	1.28E+06	3.91E+03	-2.7	1.8	14.5	4.0
Rastering (15x15)	FR9@1_63	Collected as a Powder	6.91E+08	2.11E+06	2.58E+05	7.87E+02	1.35E+06	4.13E+03	-5.9	1.7	6.2	3.9
Rastering (15x15)	FR9@1_64	Collected as a Powder	6.31E+08	1.93E+06	2.35E+05	7.18E+02	1.24E+06	3.78E+03	-3.1	1.8	5.5	4.1
Rastering (15x15)	FR9@1_65	Collected as a Powder	6.73E+08	2.05E+06	2.48E+05	7.58E+02	1.34E+06	4.09E+03	11.4	1.7	-4.7	4.0
Rastering (15x15)	FR9@1_66	Collected as a Powder	7.44E+08	2.27E+06	2.75E+05	8.41E+02	1.48E+06	4.53E+03	11.7	1.6	-2.2	3.8
Rastering (15x15)	FR9@1_67	Collected as a Powder	7.40E+08	2.26E+06	2.77E+05	8.45E+02	1.47E+06	4.50E+03	10.0	1.6	8.2	3.8
Rastering (15x15)	FR9@1_68	Collected as a Powder	7.11E+08	2.17E+06	2.62E+05	8.01E+02	1.41E+06	4.30E+03	5.2	1.7	-5.2	3.9
Rastering (15x15)	FR9@1_69	Collected as a Powder	7.05E+08	2.15E+06	2.56E+05	7.82E+02	1.41E+06	4.29E+03	11.7	1.7	-19.8	4.0
Rastering (15x15)	FR9@1_70	Collected as a Powder	7.28E+08	2.22E+06	2.70E+05	8.24E+02	1.43E+06	4.36E+03	-5.2	1.7	0.1	3.8
Rastering (15x15)	FR9@1_71	Collected as a Powder	6.96E+08	2.13E+06	2.60E+05	7.92E+02	1.37E+06	4.19E+03	-0.2	1.7	4.9	3.9
Rastering (15x15)	FR9@1_72	Collected as a Powder	6.90E+08	2.11E+06	2.57E+05	7.84E+02	1.37E+06	4.19E+03	8.2	1.7	3.4	3.9
Rastering (15x15)	FR9@1_73	Collected as a Powder	7.21E+08	2.20E+06	2.68E+05	8.19E+02	1.45E+06	4.44E+03	23.4	1.7	4.0	3.9
Rastering (15x15)	FR9@1_74	Collected as a Powder	7.39E+08	2.26E+06	2.73E+05	8.34E+02	1.48E+06	4.53E+03	18.3	1.6	-3.3	3.8

Table S3.3: Oxygen isotopic composition expressed as $\delta^{17}O$(‰) and $\delta^{18}O$(‰). The plasma discharge is generated in a mixture N_2O - Pentanol. The sample collected on the glass walls is noted *Powder*. The ionic counting rates are expressed in counts per second (cps) while the total number of counts (Tot) depend on the duration of the measurement. The average value of the PDCM is used as the reference value for calculating the δ values of the hotspots exhibiting marked departure in their isotopic composition. The ionic ratios $^{17}O/^{16}O$ and $^{18}O/^{16}O$ used to calculate the δ values are indicated as *Reference Std value*. They correspond to the average values determined on the PDCM noted FR9 in this Table. Error bars are the statistical precision calculated on the total number of counts ($\pm 2\sigma$). Three examples of the statistical distribution of the data is shown for (1) an olivine sample (San Carlos) (2) a terrestrial kerogen (noted D. Rumble) for which the $\delta^{17}O$ and $\delta^{18}O$(‰) were determined relative to SMOW (≈+0.5 and ≈+1.0 ‰, respectively) (3) one region of the sample (noted PDCM) showing a statistical distribution of isotope ratios. The PDCM distribution is reported in Figure S3.3 bellow.

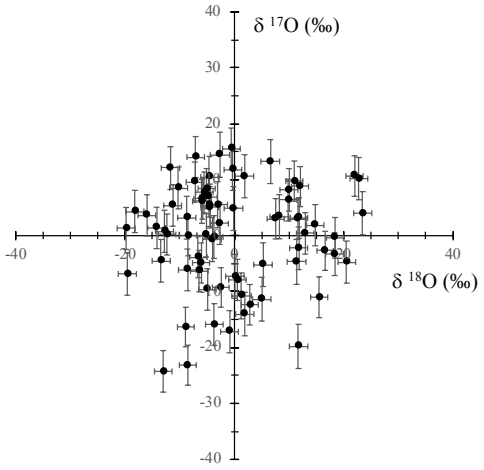

Figure S3.3: An example of the distribution of data recorded randomly on the PDCM is shown as $\delta^{17}O$ (‰) *vs.* $\delta^{18}O$ (‰). *Samples FR9@1* in Table S3.3. The reproducibility on the average is ±21.7 and ±18.4 (2σ) on $\delta^{17}O$ (‰) and $\delta^{18}O$ (‰), respectively. Error bars stand for the statistical analytical error. The statistical error bars depend only on the total number of ions detected. These error bars do not overlap 0-0‰ because the stochastic distribution of the data caused by topographic effects exceeds by far this statistical error.

S3.4:

Faraday on 16O, EM on 17O and 18O
Pentanol / N2O

17O/16O PDCM used as the reference = 3.709E-04
18O/16O PDCM used as the reference = 1.972E-03

	Sample	Comments	16O Tot.	16O Cps	17O Tot.	17O Cps	18O Tot.	18O Cps	Delta 18 ‰	± 18 (2s) ‰	Delta 17 ‰	±17 (2s) ‰
Depth Profiling	FR12@2_66	Area 1 in PDCM Powder	4.53E+08	1.38E+06	1.58E+05	4.81E+02	8.09E+05	2.47E+03	-94.0	2.2	-61.8	5.0
Depth Profiling	FR12@2_67	Area 1 in PDCM Powder	1.03E+09	3.13E+06	2.73E+05	8.34E+02	1.42E+06	4.35E+03	-294.9	1.7	-280.9	3.8
Depth Profiling	FR12@2_68	Area 1 in PDCM Powder	8.95E+08	2.73E+06	2.34E+05	7.13E+02	1.24E+06	3.77E+03	-299.8	1.8	-296.0	4.1
Depth Profiling	FR12@2_69	Area 1 in PDCM Powder	7.91E+08	2.41E+06	1.88E+05	5.75E+02	9.96E+05	3.04E+03	-361.6	2.0	-358.1	4.6
Depth Profiling	FR12@2_70	Area 1 in PDCM Powder	7.31E+08	2.23E+06	1.71E+05	5.22E+02	9.10E+05	2.78E+03	-368.2	2.1	-368.6	4.8
Depth Profiling	FR12@4_1	Area 2 in PDCM Powder	7.34E+08	2.24E+06	2.34E+05	7.13E+02	1.19E+06	3.64E+03	-176.2	1.8	-142.1	4.1
Depth Profiling	FR12@4_2	Area 2 in PDCM Powder	1.26E+09	3.85E+06	4.05E+05	1.24E+03	2.08E+06	6.34E+03	-165.1	1.4	-135.5	3.1
Depth Profiling	FR12@4_3	Area 2 in PDCM Powder	1.60E+09	4.90E+06	5.45E+05	1.66E+03	2.86E+06	8.71E+03	-97.2	1.2	-84.5	2.7
Depth Profiling	FR12@8_1	Area 4 in PDCM Powder	1.19E+09	3.64E+06	3.30E+05	1.01E+03	1.70E+06	5.19E+03	-276.4	1.5	-254.8	3.5
Depth Profiling	FR12@8_2	Area 4 in PDCM Powder	1.61E+09	4.91E+06	4.72E+05	1.44E+03	2.44E+06	7.44E+03	-232.2	1.3	-210.3	2.9
Depth Profiling	FR12@8_3	Area 4 in PDCM Powder	1.18E+09	3.62E+06	3.73E+05	1.14E+03	1.93E+06	5.88E+03	-174.7	1.4	-150.6	3.3
Depth Profiling	FR12@8_4	Area 4 in PDCM Powder	1.15E+09	3.52E+06	3.43E+05	1.05E+03	1.80E+06	5.50E+03	-208.0	1.5	-197.2	3.4
Depth Profiling	FR12@8_5	Area 4 in PDCM Powder	1.36E+09	4.15E+06	4.26E+05	1.30E+03	2.24E+06	6.85E+03	-162.3	1.3	-154.9	3.1

Table S3.4: Oxygen isotopic composition expressed as $\delta^{17}O$(‰) and $\delta^{18}O$(‰). The plasma discharge is generated in a mixture N_2O - Pentanol. The sample collected on the glass walls is noted *Powder*. The ionic counting rates are expressed in counts per second (cps) while the total number of counts (Tot) depend on the duration of the measurement. The ionic ratios $^{17}O/^{16}O$ and $^{18}O/^{16}O$ used to calculate the δ values are indicated as *PDCM used as the reference*. They correspond to the average values determined on the PDCM noted FR9 (cf. previous Table S3.3). Error bars are the statistical precision calculated on the total number of counts (±2σ). No hotspot (i.e. no increase in the ionic intensities) is observed at the location (noted *Area*) where MIF effect was measured. This Table was used to construct the Figure 2 of the text.

S3.5:

EM on 16O, 17O and 18O
MgCl2 in Pentanol / CO2

17O/16O PDCM used as the reference = 3.717E-04
18O/16O PDCM used as the reference = 2.130E-03

FR35	Sample	Comments	16O Tot.	16O Cps	17O Tot.	17O Cps	18O Tot.	18O Cps	Delta 18 ‰	± 18 (2s) ‰	Delta 17 ‰	±17 (2s) ‰
Hot Spot 2	Robert-Juillet-2020_4.im	Hot Spot on Si Wafer	1.75E+06	6.40E+04	8.87E+02	3.25E+01	5.10E+03	1.86E+02	367.3	14.0	364.1	33.6
Hot Spot 4	Robert-Juillet-2020_4.im	Hot Spot on Si Wafer	6.34E+05	1.30E+05	2.47E+02	5.06E+01	1.37E+03	2.81E+02	14.7	27.0	48.4	63.6
Hot Spot 5	Robert-Juillet-2020_4.im	Hot Spot on Si Wafer	1.81E+06	5.85E+04	7.09E+02	2.29E+01	3.99E+03	1.29E+02	32.7	15.8	52.6	37.6
Hot Spot 7	Robert-Juillet-2020_5.im	Hot Spot on Si Wafer	1.60E+06	3.79E+04	6.51E+02	1.54E+01	3.49E+03	8.28E+01	25.7	16.9	95.2	39.2
Hot Spot 8	Robert-Juillet-2020_5.im	Hot Spot on Si Wafer	2.10E+06	6.49E+04	7.95E+02	2.46E+01	4.39E+03	1.36E+02	-18.8	15.1	18.5	35.5
Hot Spot 9	Robert-Juillet-2020_5.im	Hot Spot on Si Wafer	3.43E+06	8.49E+04	1.34E+03	3.33E+01	6.98E+03	1.73E+02	-44.2	12.0	55.4	27.3
Hot Spot 6	Robert-Juillet-2020_5.im	Hot Spot on Si Wafer	1.59E+06	1.09E+04	7.06E+02	4.86E+00	3.73E+03	2.57E+01	106.1	16.4	198.4	37.6
Hot Spot Outside	Robert-Juillet-2020_9.im	Hot Spot on Si Wafer	8.49E+06	8.94E+02	3.92E+03	4.13E-01	2.17E+04	2.29E+00	202.6	6.8	243.2	16.0
4 Hot Spots	Robert-Juillet-2020_9.im	Hot Spot on Si Wafer	1.39E+06		6.43E+02		3.46E+03		163.9	17.0	240.9	39.4
Hot Spot	Robert-Juillet-2020_9.im	Hot Spot on Si Wafer	3.34E+06	3.91E+02	1.61E+03	1.88E-01	9.12E+03	1.07E+00	280.3	10.5	294.2	24.9
Bulk Image	Robert-Juillet-2020_9.im	On Si Wafer	1.88E+07	2.07E+03	8.01E+03	8.82E-01	4.49E+04	4.94E+00	122.8	4.7	148.8	11.2

FR35	Sample	Comments	16O Tot.	16O Cps	17O Tot.	17O Cps	18O Tot.	18O Cps	Delta 18 ‰	± 18 (2s) ‰	Delta 17 ‰	±17 (2s) ‰
Random Area 1	Robert-Juillet-2020_10.im	On Si Wafer	1.38E+06	4.45E+03	9.23E+02	2.98E+00	7.02E+03	2.26E+01	1390.5	11.9	801.4	32.9
Random Area 2	Robert-Juillet-2020_10.im	On Si Wafer	5.00E+05	1.61E+03	3.26E+02	1.05E+00	2.21E+03	7.14E+00	1078.0	21.3	754.2	55.4
Random Area 3	Robert-Juillet-2020_10.im	On Si Wafer	5.70E+05	1.84E+03	3.64E+02	1.17E+00	2.82E+03	9.10E+00	1323.8	18.8	718.2	52.4
Random Area 4	Robert-Juillet-2020_10.im	On Si Wafer	2.55E+06	8.23E+03	1.55E+03	5.00E+00	1.11E+04	3.59E+01	1048.0	9.5	632.7	25.4
Random Area 5	Robert-Juillet-2020_10.im	On Si Wafer	1.71E+06	5.50E+03	1.01E+03	3.27E+00	7.32E+03	2.36E+01	1013.1	11.7	598.7	31.4
Random Area 6	Robert-Juillet-2020_10.im	On Si Wafer	1.25E+06	4.03E+03	7.93E+02	2.56E+00	5.79E+03	1.87E+01	1177.4	13.1	708.4	35.5
Random Area 7	Robert-Juillet-2020_10.im	On Si Wafer	2.42E+06	7.80E+03	1.50E+03	4.85E+00	9.58E+03	3.09E+01	860.2	10.2	671.8	25.8
Random Area 8	Robert-Juillet-2020_10.im	On Si Wafer	1.18E+06	3.82E+03	6.85E+02	2.21E+00	4.34E+03	1.40E+01	724.6	15.2	558.4	38.2
Random Area 9	Robert-Juillet-2020_10.im	On Si Wafer	9.73E+05	3.14E+03	5.47E+02	1.76E+00	3.72E+03	1.20E+01	796.6	16.4	512.6	42.8
Random Area 4	Robert-Juillet-2020_17.im	On Si Wafer	5.49E+06	1.58E+04	2.29E+03	6.59E+00	1.23E+04	3.56E+01	55.7	9.0	119.4	20.9

FR35	Sample	Comments	16O Tot.	16O Cps	17O Tot.	17O Cps	18O Tot.	18O Cps	Delta 18 ‰	± 18 (2s) ‰	Delta 17 ‰	±17 (2s) ‰
Hot Spot 1	Robert-Juillet-2020_17.im	Hot Spot on Si Wafer	1.93E+06	2.62E+05	9.80E+02	1.33E+02	4.73E+03	6.41E+02	149.0	14.5	364.2	31.9
Hot Spot 2	Robert-Juillet-2020_17.im	Hot Spot on Si Wafer	2.62E+05	4.50E+04	2.09E+02	3.59E+01	1.25E+03	2.15E+02	1240.9	28.3	1145.3	69.2
Hot Spot 3	Robert-Juillet-2020_17.im	Hot Spot on Si Wafer	1.14E+07	4.11E+05	5.27E+03	1.89E+02	2.60E+04	9.34E+02	65.8	6.2	237.5	13.8
Hot Spot 5	Robert-Juillet-2020_17.im	Hot Spot on Si Wafer	4.47E+06	3.45E+05	1.98E+03	1.53E+02	1.03E+04	7.93E+02	79.4	9.9	193.0	22.5
Hot Spot 7	Robert-Juillet-2020_17.im	Hot Spot on Si Wafer	7.20E+06	3.57E+05	3.12E+03	1.55E+02	1.63E+04	8.07E+02	61.4	7.8	167.0	17.9
Hot Spot 8	Robert-Juillet-2020_17.im	Hot Spot on Si Wafer	8.46E+06	3.45E+05	3.59E+03	1.46E+02	1.83E+04	7.48E+02	18.3	7.4	142.4	16.7
Hot Spot 9	Robert-Juillet-2020_17.im	Hot Spot on Si Wafer	6.01E+05	4.66E+04	3.60E+02	2.79E+01	2.14E+03	1.66E+02	669.3	21.6	613.0	52.7
Hot Spot 10	Robert-Juillet-2020_17.im	Hot Spot on Si Wafer	1.28E+06	1.08E+05	6.18E+02	5.20E+01	3.36E+03	2.83E+02	231.3	17.2	296.7	40.2
Hot Spot 11	Robert-Juillet-2020_17.im	Hot Spot on Si Wafer	1.57E+06	1.82E+05	7.54E+02	8.73E+01	3.79E+03	4.38E+02	132.3	16.2	291.6	36.4
Hot Spot 12	Robert-Juillet-2020_17.im	Hot Spot on Si Wafer	1.13E+06	2.58E+05	5.17E+02	1.18E+02	2.77E+03	6.33E+02	151.8	19.0	231.5	44.0
Hot Spot 13	Robert-Juillet-2020_17.im	Hot Spot on Si Wafer	2.29E+05	9.54E+04	1.61E+02	6.71E+01	8.88E+02	3.70E+02	820.4	33.6	891.3	78.8
Random Area 5	Robert-Juillet-2020_17.im	On Si Wafer	5.36E+06	1.55E+04	2.31E+03	6.67E+00	1.22E+04	3.52E+01	69.3	9.0	160.3	20.8
Random Area 6	Robert-Juillet-2020_17.im	On Si Wafer	2.34E+07	6.74E+04	1.01E+04	2.91E+01	5.32E+04	1.54E+02	69.9	4.3	159.5	10.0
Random Area 7	Robert-Juillet-2020_17.im	On Si Wafer	6.42E+06	1.85E+04	3.04E+03	8.78E+00	1.64E+04	4.74E+01	200.0	7.8	274.0	18.1
Random Area 8	Robert-Juillet-2020_17.im	On Si Wafer	3.32E+06	9.57E+03	1.50E+03	4.31E+00	8.38E+03	2.42E+01	186.2	10.9	212.8	25.9
Random Area 9	Robert-Juillet-2020_17.im	On Si Wafer	2.84E+07	8.20E+04	1.26E+04	3.64E+01	6.55E+04	1.89E+02	82.8	3.9	196.0	8.9
Hot Spot 6	Robert-Juillet-2020_17.im	Hot Spot on Si Wafer	8.52E+06	2.55E+05	3.50E+03	1.05E+02	1.83E+04	5.48E+02	9.5	7.4	106.4	16.9
Random Area 2	Robert-Juillet-2020_17.im	On Si Wafer	1.05E+07	3.03E+04	4.28E+03	1.23E+01	2.26E+04	6.52E+01	9.6	6.7	94.3	15.3
Hot Spot 4	Robert-Juillet-2020_17.im	Hot Spot on Si Wafer	7.32E+06	3.09E+05	3.09E+03	1.31E+02	1.59E+04	6.72E+02	19.3	7.9	135.8	18.0
Random Area 3	Robert-Juillet-2020_17.im	On Si Wafer	3.69E+07	1.06E+05	1.52E+04	4.39E+01	7.90E+04	2.28E+02	6.1	3.6	110.6	8.1

FR35	Sample	Comments	16O Tot.	16O Cps	17O Tot.	17O Cps	18O Tot.	18O Cps	Delta 18 ‰	± 18 (2s) ‰	Delta 17 ‰	±17 (2s) ‰
Hot Spot 3	Robert-Juillet-2020_18.im	Hot Spot on Si Wafer	8.71E+06	1.54E+05	3.74E+03	6.59E+01	1.91E+04	3.36E+02	27.4	7.2	155.6	16.3
Hot Spot 8	Robert-Juillet-2020_18.im	Hot Spot on Si Wafer	5.75E+06	1.25E+05	2.59E+03	5.64E+01	1.33E+04	2.89E+02	85.1	8.7	214.2	19.6
Hot Spot 10	Robert-Juillet-2020_18.im	Hot Spot on Si Wafer	1.42E+06	1.68E+05	6.33E+02	7.47E+01	3.14E+03	3.70E+02	34.1	17.9	195.8	39.7
Hot Spot 11	Robert-Juillet-2020_18.im	Hot Spot on Si Wafer	4.26E+06	1.24E+05	1.85E+03	5.38E+01	9.45E+03	2.75E+02	41.7	10.3	168.1	23.3
Hot Spot 13	Robert-Juillet-2020_18.im	Hot Spot on Si Wafer	3.35E+06	9.33E+04	1.54E+03	4.30E+01	7.75E+03	2.16E+02	85.4	11.4	239.0	25.4
Hot Spot 15	Robert-Juillet-2020_18.im	Hot Spot on Si Wafer	2.18E+06	8.59E+04	9.78E+02	3.85E+01	4.92E+03	1.94E+02	58.2	14.3	205.9	32.0
Hot Spot 16	Robert-Juillet-2020_18.im	Hot Spot on Si Wafer	4.29E+06	1.39E+05	1.91E+03	6.18E+01	9.54E+03	3.09E+02	43.9	10.2	195.3	22.9
Hot Spot 17	Robert-Juillet-2020_18.im	Hot Spot on Si Wafer	2.79E+06	5.33E+04	1.22E+03	2.32E+01	6.25E+03	1.19E+02	51.1	12.7	174.2	28.7
Hot Spot 21	Robert-Juillet-2020_18.im	Hot Spot on Si Wafer	9.50E+06	3.18E+04	4.20E+03	1.41E+01	2.20E+04	7.38E+01	89.4	6.7	190.1	15.4
Hot Spot 22	Robert-Juillet-2020_18.im	Hot Spot on Si Wafer	5.28E+06	3.10E+04	2.33E+03	1.37E+01	1.20E+04	7.03E+01	64.1	9.1	186.7	20.7
Randomm Area 10	Robert-Juillet-2020_18.im	On Si Wafer	1.94E+07	6.18E+04	8.59E+03	2.73E+01	4.47E+04	1.42E+02	79.2	4.7	188.9	10.8
Randomm Area 11	Robert-Juillet-2020_18.im	On Si Wafer	9.60E+06	3.05E+04	4.13E+03	1.31E+01	2.16E+04	6.87E+01	57.3	6.8	157.9	15.6
Randomm Area 12	Robert-Juillet-2020_18.im	On Si Wafer	1.65E+07	5.24E+04	7.43E+03	2.36E+01	3.83E+04	1.22E+02	91.2	5.1	213.5	11.6
Randomm Area 13	Robert-Juillet-2020_18.im	On Si Wafer	1.43E+07	4.54E+04	6.00E+03	1.91E+01	3.16E+04	1.00E+02	37.2	5.6	129.5	12.9
Randomm Area 14	Robert-Juillet-2020_18.im	On Si Wafer	1.61E+07	5.13E+04	6.79E+03	2.16E+01	3.61E+04	1.15E+02	51.2	5.3	131.6	12.1
Randomm Area 15	Robert-Juillet-2020_18.im	On Si Wafer	2.38E+07	7.58E+04	1.03E+04	3.26E+01	5.24E+04	1.66E+02	31.7	4.4	157.4	9.9
Randomm Area 16	Robert-Juillet-2020_18.im	On Si Wafer	6.13E+06	1.95E+04	2.73E+03	8.67E+00	1.47E+04	4.68E+01	127.9	8.2	197.6	19.1
Randomm Area 17	Robert-Juillet-2020_18.im	On Si Wafer	1.07E+07	3.40E+04	4.80E+03	1.53E+01	2.52E+04	8.01E+01	105.3	6.3	205.5	14.4
Randomm Area 18	Robert-Juillet-2020_18.im	On Si Wafer	1.21E+07	3.85E+04	5.34E+03	1.70E+01	2.80E+04	8.90E+01	84.6	6.0	184.2	13.7
Randomm Area 19	Robert-Juillet-2020_18.im	On Si Wafer	1.03E+07	3.28E+04	4.58E+03	1.45E+01	2.34E+04	7.45E+01	67.7	6.5	194.3	14.8
Randomm Area 20	Robert-Juillet-2020_18.im	On Si Wafer	7.59E+06	2.41E+04	3.63E+03	1.15E+01	1.79E+04	5.68E+01	105.8	7.5	286.6	16.6
Randomm Area 21	Robert-Juillet-2020_18.im	On Si Wafer	4.20E+06	1.34E+04	1.90E+03	6.03E+00	1.03E+04	3.27E+01	149.1	9.9	216.1	22.9
Randomm Area 22	Robert-Juillet-2020_18.im	On Si Wafer	7.27E+06	2.31E+04	3.41E+03	1.08E+01	1.79E+04	5.69E+01	156.4	7.5	263.5	17.1
Randomm Area 23	Robert-Juillet-2020_18.im	On Si Wafer	7.86E+06	2.50E+04	3.50E+03	1.11E+01	1.88E+04	5.98E+01	124.5	7.3	199.9	16.9
Randomm Area 24	Robert-Juillet-2020_18.im	On Si Wafer	9.66E+06	3.07E+04	4.43E+03	1.41E+01	2.31E+04	7.33E+01	121.1	6.6	232.5	15.0
Randomm Area 25	Robert-Juillet-2020_18.im	On Si Wafer	7.39E+06	2.35E+04	3.44E+03	1.09E+01	1.69E+04	5.36E+01	70.9	7.7	254.0	17.0
Hot Spot 4	Robert-Juillet-2020_18.im	Hot Spot on Si Wafer	5.52E+06	1.38E+05	2.22E+03	5.54E+01	1.15E+04	2.88E+02	-19.8	9.3	81.1	21.2
Hot Spot 9	Robert-Juillet-2020_18.im	Hot Spot on Si Wafer	3.51E+06	1.15E+05	1.45E+03	4.76E+01	7.47E+03	2.46E+02	0.5	11.6	110.4	26.3
Hot Spot 12	Robert-Juillet-2020_18.im	Hot Spot on Si Wafer	2.08E+06	9.00E+04	8.44E+02	3.65E+01	4.52E+03	1.95E+02	19.4	14.9	91.2	34.4
Hot Spot 14	Robert-Juillet-2020_18.im	Hot Spot on Si Wafer	3.37E+06	1.08E+05	1.33E+03	4.27E+01	7.14E+03	2.29E+02	-5.9	11.8	60.2	27.4
Hot Spot 19	Robert-Juillet-2020_18.im	Hot Spot on Si Wafer	3.09E+06	1.11E+05	1.23E+03	4.40E+01	6.55E+03	2.34E+02	-5.6	12.4	69.8	28.5
Hot Spot 5	Robert-Juillet-2020_18.im	Hot Spot on Si Wafer	3.35E+06	1.37E+05	1.33E+03	5.45E+01	7.34E+03	3.00E+02	27.7	11.7	67.6	27.4
Hot Spot 18	Robert-Juillet-2020_18.im	Hot Spot on Si Wafer	1.46E+06	7.65E+04	5.91E+02	3.09E+01	3.30E+03	1.73E+02	59.1	17.4	87.3	41.1
Randomm Area 1	Robert-Juillet-2020_18.im	On Si Wafer	4.39E+06	1.40E+04	1.84E+03	5.85E+00	9.38E+03	2.98E+01	3.3	10.3	128.1	23.3
Randomm Area 2	Robert-Juillet-2020_18.im	On Si Wafer	9.83E+06	3.12E+04	4.08E+03	1.30E+01	2.13E+04	6.78E+01	19.9	6.8	117.2	15.7
Randomm Area 3	Robert-Juillet-2020_18.im	On Si Wafer	2.17E+06	6.90E+03	8.90E+02	2.83E+00	4.90E+03	1.56E+01	59.6	14.3	102.2	33.5
Randomm Area 5	Robert-Juillet-2020_18.im	On Si Wafer	1.16E+07	3.68E+04	4.88E+03	1.55E+01	2.58E+04	8.19E+01	43.3	6.2	132.6	14.3
Randomm Area 6	Robert-Juillet-2020_18.im	On Si Wafer	1.55E+07	4.93E+04	6.51E+03	2.07E+01	3.42E+04	1.09E+02	35.7	5.4	129.0	12.4
Randomm Area 7	Robert-Juillet-2020_18.im	On Si Wafer	1.90E+07	6.02E+04	7.99E+03	2.54E+01	4.18E+04	1.33E+02	36.2	4.9	134.1	11.2
Randomm Area 8	Robert-Juillet-2020_18.im	On Si Wafer	3.60E+06	1.14E+04	1.52E+03	4.84E+00	8.00E+03	2.54E+01	42.6	11.2	137.3	25.6
Randomm Area 9	Robert-Juillet-2020_18.im	On Si Wafer	1.62E+07	5.15E+04	6.75E+03	2.15E+01	3.52E+04	1.12E+02	18.3	5.3	120.8	12.2
Hot Spot 6	Robert-Juillet-2020_18.im	Hot Spot on Si Wafer	3.85E+06	1.16E+05	1.60E+03	4.82E+01	8.32E+03	2.51E+02	15.7	11.0	118.0	25.0
Hot Spot 7	Robert-Juillet-2020_18.im	Hot Spot on Si Wafer	5.61E+06	9.14E+04	2.35E+03	3.84E+01	1.25E+04	2.04E+02	46.1	8.9	129.4	20.6
Hot Spot 20	Robert-Juillet-2020_18.im	Hot Spot on Si Wafer	2.99E+06	4.75E+04	1.26E+03	2.01E+01	6.72E+03	1.07E+02	56.6	12.2	136.3	28.2
Randomm Area 4	Robert-Juillet-2020_18.im	On Si Wafer	1.80E+06	5.71E+03	7.56E+02	2.40E+00	4.04E+03	1.28E+01	55.5	15.7	131.3	36.4
Hot Spot 1	Robert-Juillet-2020_18.im	Hot Spot on Si Wafer	7.57E+06	2.40E+05	3.19E+03	1.01E+02	1.65E+04	5.21E+02	21.0	7.8	135.2	17.7
Hot Spot 2	Robert-Juillet-2020_18.im	Hot Spot on Si Wafer	9.46E+06	1.93E+05	3.93E+03	8.01E+01	2.05E+04	4.17E+02	17.5	7.0	118.6	15.9

Table S3.5: Oxygen isotopic composition expressed as $\delta^{17}O$(‰) and $\delta^{18}O$(‰). The plasma discharge is generated in a mixture $MgCl_2$ - Pentanol - CO_2. The sample is collected on a silicon wafer. The ionic counting rates are expressed in counts per second (cps) while the total number of counts (Tot.) depends on the duration of the measurement. The ionic ratios $^{17}O/^{16}O$ and $^{18}O/^{16}O$ of the PDCM used to calculate the δ values are indicated as *Reference Std values.* The area of the PDCM is defined on the same wafer where isotopic hotspots were measured. In absence of identifiable hotspots in an ion image, the raster area (20×20 μm) was divided in 9 *Random Areas*. *Bulk* is the measured (not calculated) average of these 9 areas. Note that isotopic effects are detectable even in hotspot free areas. This Table was used to construct the Figure 2 of the text. All sample names correspond to files registered in the NanoSims data files.

S4. Calculated MIF slopes in a 3 isotope diagram

Several theories have been developed to account for the MIF effect[6,16, 25-30]. They were all based on the results obtained on the isotopic composition of ozone for which numerous and precise laboratory parameters are available in the literature. They are centered on the interpretation of the empirical fit (the η factor) discovered experimentally by Janssen[2], which accounts for the isotopic compositions of the different isotopomers of ozone:

$$\alpha = \alpha_{MDF} \cdot \eta$$

The η factor referred here to as the MIF factor (Mass Independent Fractionation factor) illustrates the fact that, for any isotopomer masses, there is a constant shift between the observed fractionation and the expected MDF factors α_{MDF}'s. The origin of η will be discussed elsewhere. Whatever its origin, η characterizes the reaction rate ratio of complexes having different symmetry such as $[^{16}O\ldots^{17}O]^*/[^{16}O\ldots^{16}O]^*$. Neglecting the MDF (i.e. α_{MDF}'s=1), and extending this ratio to all possible isotopic reactions for a given chemical element gives the overall mass independent isotopic fractionation factor $^{m\text{-}16}\alpha$[18]:

$$^{m-16}\alpha = \frac{1+x(m)[\eta^{-1}-1]}{1+x(16)[\eta^{-1}-1]}$$

m designates 17 or 18 and *x(16), x(17)* and *x(18)* stand for the relative abundances of ^{16}O, ^{17}O and ^{18}O (i.e. 99.76 x10^{-2}, 380 x10^{-6} and 2000 x10^{-6} respectively). Note that, in this formalism, the isotopic fractionation factor is not anymore the rate constant ratio, but instead the reaction rate ratio. In the 3 isotope diagram, the slope $\Delta(\delta^{17}O)/\Delta(\delta^{18}O)$ depends only on the relative abundances of the 3 isotopes with no free parameters.

Taking the example of magnesium isotopes (X(24)=0.7899, x(25)= 0.100, x(26)=0.11), the slope $\Delta(\delta^{25}Mg)/\Delta(\delta^{26}O)$= 0.985, $\forall(\Delta\eta)$. A detailed theoretical treatment of the MIF effect is proposed in *Chem. Phys.* (in press).

S5. Details of the Pentane/N_2O analyses.

	delta 18		delta 17	
	‰	±2s	‰	±2s
FR12- 8_1	-306	19.7	-294	27.1
FR12- 8_1	-306	19.7	-287	27.0
FR12- 8_1	-298	19.7	-269	26.9
FR12- 8_1	-288	19.7	-274	26.9
FR12- 8_1	-287	19.7	-266	26.8
FR12- 8_1	-286	19.7	-259	26.7
FR12- 8_1	-274	19.6	-252	26.7
FR12- 8_1	-277	19.6	-245	26.6
FR12- 8_1	-268	19.6	-244	26.6
FR12- 8_1	-268	19.6	-243	26.6
FR12- 8_1	-261	19.6	-242	26.6
FR12- 8_1	-267	19.6	-251	26.6
FR12- 8_1	-267	19.6	-249	26.6
FR12- 8_1	-267	19.6	-255	26.7
FR12- 8_1	-272	19.6	-239	26.6
FR12- 8_1	-268	19.6	-243	26.6
FR12- 8_1	-267	19.6	-247	26.6
FR12- 8_1	-264	19.6	-246	26.7
FR12- 8_1	-267	19.6	-247	26.7
FR12- 8_1	-273	19.6	-247	26.7
FR12- 8_2	-143	19.2	-126	25.2
FR12- 8_2	-143	19.2	-120	25.2
FR12- 8_2	-149	19.2	-117	25.2
FR12- 8_2	-148	19.2	-124	25.2
FR12- 8_2	-151	19.3	-126	25.2
FR12- 8_2	-154	19.3	-121	25.2
FR12- 8_2	-154	19.3	-134	25.3
FR12- 8_2	-158	19.3	-132	25.3
FR12- 8_2	-159	19.3	-139	25.3
FR12- 8_2	-159	19.3	-132	25.3
FR12- 8_2	-164	19.3	-148	25.4
FR12- 8_2	-160	19.3	-146	25.4
FR12- 8_2	-160	19.3	-132	25.3
FR12- 8_2	-162	19.3	-134	25.3
FR12- 8_2	-168	19.3	-159	25.4
FR12- 8_2	-167	19.3	-134	25.4
FR12- 8_2	-168	19.3	-143	25.4
FR12- 8_2	-169	19.3	-137	25.4
FR12- 8_2	-170	19.3	-148	25.4
FR12- 8_2	-169	19.3	-141	25.4

	delta 18		delta 17	
	‰	±2s	‰	±2s
FR12-8_3	-151	19.4	-136	25.9
FR12-8_3	-163	19.5	-127	26.0
FR12-8_3	-159	19.5	-136	26.0
FR12-8_3	-160	19.5	-154	26.1
FR12-8_3	-174	19.5	-150	26.1
FR12-8_3	-172	19.5	-144	26.1
FR12-8_3	-173	19.5	-143	26.1
FR12-8_3	-179	19.5	-156	26.2
FR12-8_3	-178	19.5	-145	26.1
FR12-8_3	-177	19.5	-142	26.1
FR12-8_3	-179	19.5	-162	26.2
FR12-8_3	-181	19.5	-156	26.2
FR12-8_3	-181	19.5	-161	26.2
FR12-8_3	-186	19.5	-157	26.2
FR12-8_3	-184	19.5	-168	26.3
FR12-8_3	-188	19.5	-159	26.3
FR12-8_3	-184	19.5	-158	26.3
FR12-8_3	-190	19.5	-168	26.3
FR12-8_3	-189	19.5	-159	26.3
FR12-8_3	-186	19.5	-172	26.4
FR12-8_4	-191	19.5	-170	26.1
FR12-8_4	-195	19.5	-186	26.3
FR12-8_4	-201	19.5	-192	26.3
FR12-8_4	-203	19.5	-175	26.3
FR12-8_4	-209	19.5	-194	26.4
FR12-8_4	-207	19.5	-191	26.4
FR12-8_4	-213	19.6	-204	26.5
FR12-8_4	-213	19.6	-207	26.5
FR12-8_4	-211	19.6	-194	26.4
FR12-8_4	-222	19.6	-201	26.5
FR12-8_4	-218	19.6	-211	26.6
FR12-8_4	-221	19.6	-218	26.6
FR12-8_4	-219	19.6	-222	26.7
FR12-8_4	-226	19.6	-227	26.7
FR12-8_4	-228	19.6	-224	26.7
FR12-8_4	-227	19.6	-229	26.7
FR12-8_4	-231	19.6	-222	26.7
FR12-8_4	-232	19.6	-220	26.7
FR12-8_4	-236	19.6	-212	26.7
FR12-8_4	-240	19.6	-230	26.8

Table S5: Pentanol/N_2O experiment. $\delta^{17,18}O$ measured by depth profiling at the location of the isotopic MIF hotspots. No hotspot in ion intensities was observed at the location of the isotopic MIF hotspots. Each step represents a sputtered thickness between 200 and 300 nm. Data are reported in the Figure S5 bellow.

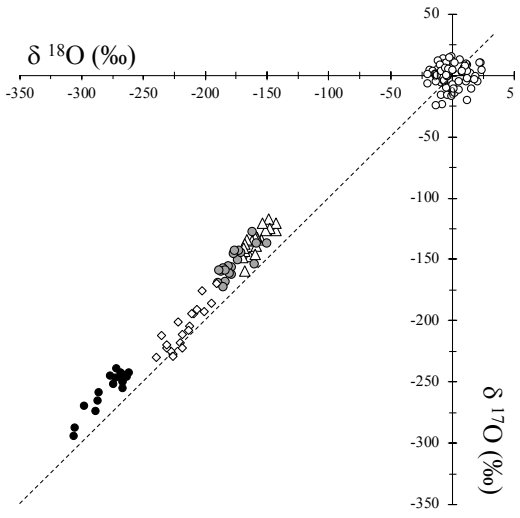

Figure S5: The $\delta^{17,18}O$ values reported for the samples FR12@8 from 1 to 4 in Table S3.4 are average values of ≈80 measurements for each sample. This figure shows the evolution of the $\delta^{17,18}O$ values averaged every 4 measurements. The PDCM used as a reference value for δ units is shown for comparison (cf. Table S3.3; open dots around 0-0‰). Black dots, open diamonds, grey dots and open triangle stand for FR12@ 8 from 1 to 4, respectively. Error bars (statistic and PDCM reproducibility) are not shown for clarity but never exceed ±19 and ±26 ‰ (2σ) for $\delta^{18}O$ and $\delta^{17}O$, respectively. The 1:1 line is drawn for reference. Note that the correlation defined by the data do not intercept the reference at 0-0‰. This may be caused by an analytical "matrix effect" but may also reflects a combined MDF and MIF effect.

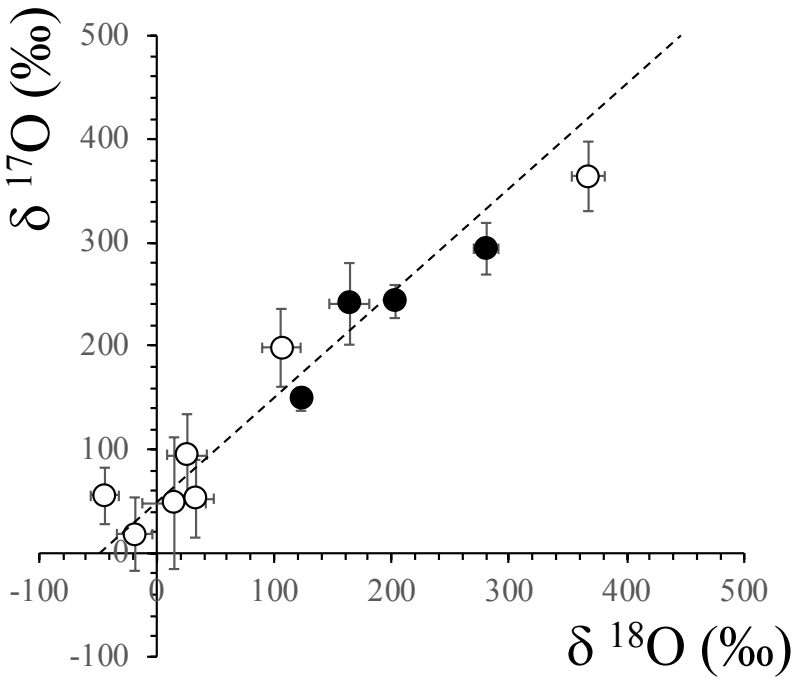

Figure S6: The $\delta^{17,18}O$ of individual emissivity hotspot measured in 3 different images: *Robert-Juillet-2020_4, _5 and _9* reported in Table S3.5. Black dots stand for the same *image 9*. The purpose of this plot is to show that the internal variations between hotspots being recorded in the same image, cannot result from bias in the instrumental setups. The dashed line is the reference 1:1 correlation line. The corresponding emissivity hotspots from *image 9* is shown in the Fig. 2b of the text.